A MeerKAT morphological and spectral index study of M 87

By

Leon MTSHWENI

UNIVERSITEIT VAN PRETORIA
UNIVERSITY OF PRETORIA
YUNIBESITHI YA PRETORIA
Denkleiers • Leading Minds • Dikgopolo tša Dihlalefi

Department of Physics
UNIVERSITY OF PRETORIA

Submitted in partial fulfilment of the requirements for the degree of MASTER OF SCIENCE (MSc) IN PHYSICS in the Faculty of Natural and Agricultural Sciences (NAS).

July 15, 2022

Supervisor: Prof. Roger DEANE and Dr. Kshitij THORAT

UNIVERSITY OF PRETORIA

Abstract

Faculty of Natural and Agricultural Sciences
Department of Physics

Master of Science (MSc) in Physics

A MeerKAT morphological and spectral index study of M 87

by Leon MTSHWENI

Supervisors: Prof. Roger DEANE and Dr. Kshitij THORAT

Messier 87 (M87) is a spectacular radio galaxy located in our cosmic backyard. Its proximity has allowed astronomers to study it in detail across the electromagnetic spectrum. M87 shows a complex structure in the radio continuum made up of a bright core, jets and a diffuse halo. High fidelity imaging of this bright ($>$ 300 Jy), complex source is necessary to understanding its evolution. MeerKAT's sensitivity and spatial resolution make it an ideal instrument to study M87's extended, diffuse radio structure. We present the MeerKAT 1.28 GHz total-intensity map, in-band spectral index image, and an analysis of its complex morphological structure. A comparison of the MeerKAT map with the VLA map is conducted, comparing all key features, by means of a two point spectral index map at the respective frequencies, 1.28 GHz and 327 MHz. Our results 1) verify the structures seen in the VLA 327 MHz image, made using maximum entropy techniques 2) show the first spectral index of the filamentary structures 3) demonstrate the ability of MeerKAT to map complex, diffuse structures at higher frequencies than before, extending the frequency range to enable for more detailed, spatially resolved spectral analysis. In conclusion, we find results that are consistent with what has been observed about M87, that it is an active galaxy with a steady spectral variation across a large radio frequency range.

Declaration of Authorship

I, Leon MTSHWENI, declare that the thesis, which I hereby submit for the degree of MSc in Physics at the University of Pretoria, is my own work and has not previously been submitted by me for a degree at this or any other tertiary institution.

Signature:

Date: July 15, 2022

Acknowledgements

This has been the most challenging part of my thesis to write, even more than the actual reduction of the MeerKAT observation. An African proverb says that it takes a village to raise a child, like wise my MSc project, which has been like a needy child, has greatly benefited from the astronomy community.

To my supervisors, Roger and Kshitij, M87 has now been on our minds for what feels like an eternity and if I never do any work on it, it would be too soon, well, unless it's some cool new UHF data, then, sign me up! Thank you both for the countless hours of remote meetings, even though about half of it was you repeating yourselves. Thank you for the continued effort you both put in throughout the years. I hope you're both proud of what we achieved, because I am.

To my colleagues at the UP-Astro group, you have all been quite instrumental in the completion of this project, thank you all. I would like to specially thank you, Thato, for your continued involvement in my project, you helped me debug my awful code far too many times, Dankie Mfanaka!

To Karabo, for being my pillar of strength. For giving me strength not to quit for what would, honestly, have been a more peaceful life. Your continued support is truly invaluable. I would not have done this without you.

We are extremely grateful to Frazer Owen for making his VLA 327 MHz map available to us for this study. The financial assistance of the South African Radio Astronomy Observatory (SARAO) towards this research is hereby acknowledged (www.ska.ac.za). We acknowledge the use of the ilifu cloud computing facility (`www.ilifu.ac.za`).

Contents

List of Figures

List of Tables

List of Abbreviations

AGN	**A**ctive **G**alactic **N**uclei.
BLR	**B**road-**L**ine **R**egions.
CASA	**C**ommon **A**stronomy **S**oftware **A**pplication.
EHT	**E**vent **H**orizon **T**elescope.
FR1	**F**anaroff-**R**iley 1.
FR2	**F**anaroff-**R**iley 2.
ICM	**I**ntra**C**luster **M**edium.
IDIA	**I**nter-University Institute for **D**ata **I**ntensive **A**stronomy.
M 87	**M**essier 87.
NLR	**N**arrow-**L**ine **R**egions.
QSO	**Q**uasi-**S**tellar **O**bjects.
RL	**R**adio-**L**oud.
rms	**r**oot **m**ean **s**quare.
RQ	**R**adio-**Q**uiet.
SMBH	**S**uper-**M**assive **B**lack-**H**ole.
SED	**S**pectral **E**nergy **D**istribution.
SR	**S**ynchrotron **R**adiation.
Sy1	**S**eyfert 1.
Sy2	**S**eyfert 2.
VLA	**V**ery **L**ong **A**rray.
VLBI	**V**ery **L**ong **B**aseline **I**nterferometry.

Chapter 1

Introduction

In the next few sections we lay the groundwork that is required in order to have a holistic understanding of M87 and the environment it sits in. We begin our journey by describing the radio sky as observed, then delve into some fundamental astrophysics of radio-loud AGN. We then describe cluster environments in the context of M87. Then finally, we discuss M87 itself and give a review of some of the work that has been performed on the radio source.

1.1 The Radio Sky

1.1.1 Active Galaxies

Active **G**alactic **N**uclei (AGN) are the very cores of galaxies, that produce copious amounts of energy from a very compact region. Galaxies that host AGN are referred to as active galaxies. AGN are, predominantly, powered by gravity, through the accretion of the surrounding matter, a process whereby matter falls onto the massive black hole at the centre of the host galaxy, converting gravitational potential energy into kinetic and thermal energy due to frictional losses. This is in contrast to the nuclear fusion that powers stars. The resulting emission is observable over a broad range in the electromagnetic spectrum.

One of the ways AGN can be classified is that of radio-loud vs radio-quiet AGN. Radio-loud AGN are strong radio emitters and usually have jets and radio extended radio lobes. The vast majority of AGN are of the radio-quiet variety. These are not vastly different objects, jets are usually the distinguishing attribute between the two classes. For this work, we focus on the radio-loud (hereafter radio galaxies) population and their associated energetics.

1.1.2 Radio galaxies

When matter accretes onto the central supermassive black hole of a galaxy, opposing twin relativistic jets of charged particles are generated from the active nucleus. These jets propagate into the medium surrounding the host galaxy and form a diffuse emission region. These are regions of low-density, high-pressure relativistic electrons that generate the observed radio emission through the non-thermal radiation process known as synchrotron radiation (Blandford et al., 2019). Based on the morphological distribution of their radio surface brightness, these galaxies are separated into two classes of objects type **F**aranoff & **R**iley I (FR-I) and **F**aranoff & **R**iley II (FR-II) (Fanaroff & Riley, 1974).

FR-I sources show higher surface brightness closer to the core, which then become fainter toward the outer extremities. In contrast, FR-II sources have well-defined jets that terminate in shocked edge-brightened cocoons. Figure 1.1 shows the prototypical FR-I and FR-II sources 3C31 and Cygnus A. It has been argued that this morphological dichotomy is due to either the associated properties in jet production mechanisms (Garofalo et al., 2010) or to the environmental factors surrounding the jets (Kaiser & Alexander, 1997). There has been evidence of radio sources displaying a mixed morphology (Gopal-Krishna & Wiita, 2000). This suggests that the FR-I/II dichotomy is at least somehow influenced by the environment.

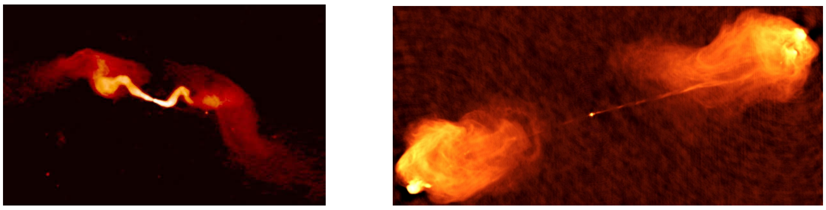

(A)
3C 31

(B) 3C 175

FIGURE 1.1: FR-I galaxies have lower power than FR-II galaxies. Left: A VLA map of the FR-I galaxy 3C31. A gradual decrease in lobe luminosity can be seen. Right: The VLA map of the FR-II galaxy Cygnus A. Edge-brightened jets that terminate in shocks. Image Credit: NRAO/AUI

There are several models that describe the dynamics of the two classes of radio-loud AGN. These FR-II and FR-I models mainly consider one limiting case in each class; i) dominating ram pressure for FR-II sources, ii) dominating external pressure for FR-I sources (Turner & Shabala, 2015).

In the next section, we explore these models in more detail.

1.1.3 Relativistic jets

The FR-II dynamical model describes a relativistic radio jet emerging from the AGN with a constant opening angle. Fig 1.2 shows a schematic diagram of a snapshot of the dynamics between the relativistic jet and its environment.

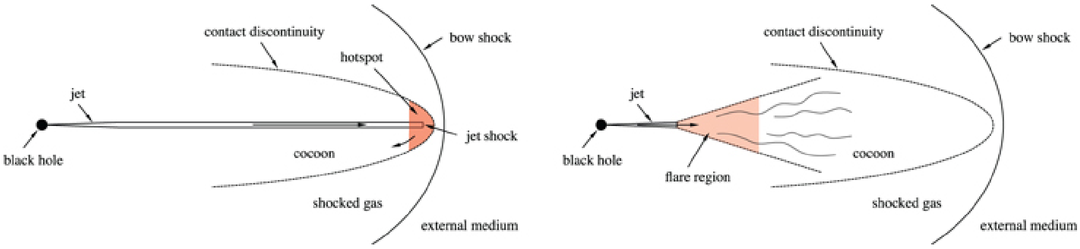

FIGURE 1.2: The (Turner & Shabala, 2015) jet models of FR-II (left) and FR-I (right) jet morphologies. This models the interactions of the radio jets with their external media. Credit: (Turner & Shabala, 2015).

The FR-II dynamical model is made up of a relativistic jet emerging from the AGN with a constant opening angle. As this jet travels it sweeps out a shock-wave in the external medium (Turner & Shabala, 2015). Eventually, a pressure balance between the jet and its cocoon develops. Due to the high speed of sound, the opening angle of the jet will remain constant since the pressure of the cocoon will remain constant, thus maintaining a concentrated beam of relativistic electrons. This, in turn, applies a higher ram pressure at the hotspot region. The jet ends in a hotspoted shock (Turner & Shabala, 2015). The ram pressure of the jet colliding with its external medium creates a bow shock. The pressure of the shocked external medium balances with the pressure exerted by the jet. The pressure in the hotspot region is higher. Then a back-flow occurs which inflates a cocoon (Turner & Shabala, 2015). Two things are important for backflow to occur 1) the ICM in which the jet propagates must be many times denser than the jet and 2) the jet needs to have very high speeds. As the jet shocks the ICM, the jet's kinetic energy is converted into thermal energy.

After the jet shock, much of the material flows outward from the jet, thus creating a hotspot. The ram-pressure of the jet is not enough to balance the pressure exerted by the ICM. This pressure imbalance then accelerates some of the material back towards the core, thus producing a backflow (Leahy & Williams, 1984). As can be seen in Fig. 1.3, the plasma flows back and reaches the z = 0 plane and accumulates into a thin disc. The black hole is modelled as a magnetically arrested disk (MAD), that is, it is assumed that a significant amount of poloidal magnetic flux collects in the vicinity of the black hole, and as a result of the continued accretion and the field remains in place around the black hole, not falling in or being blown away (Narayan et al., 2003).

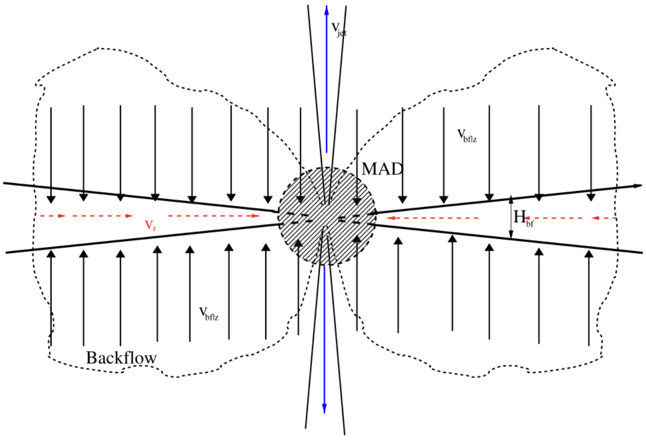

FIGURE 1.3: A model of the backflow and the effect it has on the central accretion region. The height of the backflow as a function of radius from the black hole is labelled as H_{bf}. The matter in backflow is confined to the disc, denoted as red dotted arrows (Antonuccio-Delogu et al., 2017).

The radio emission is due to the non-thermal process where the electrons in the plasma precess the magnetic field lines of the cocoon. Similar to the FR-II model, a ballistic jet emanating from the AGN inflates a cocoon. However, in this case, shocks occur much closer to the AGN. The FR-I counterpart to an FR-II hotspot is called a flare region. The diffuse emission region, which extends well beyond the shock is also called the cocoon (Turner & Shabala, 2015).

1.2 Astrophysics of radio galaxies

1.2.1 Synchrotron Spectra

When cold galactic matter falls onto the supermassive black hole that harbours it, energy is released. This occurs through the process called accretion, whereby an accretion disk is formed by diffuse material orbiting the galaxy (Longair, 2011). As matter falls onto the black hole, angular momentum is transported outwards.

Matter falling onto the black hole can follow a spiral path, this is because a turbulent flow caused by viscosity and magnetic fields raises the internal heat of the system, which in turn is converted into energy that leaves the system. Thus, reducing the angular momentum of the particles and sending particles into an inward spiral (Longair, 2011). Temperatures can be high enough to emit X-rays just outside the event horizon of the black hole.

Through these turbulent processes, particles become ionised, thus creating an electron gas or plasma. This gas/plasma then creates a magnetic field which, itself, is threaded by a net external magnetic field that exists in the ICM. As the entire galactic system rotates these magnetic fields may become tangled and typically oriented along the rotation axis of the system (Longair, 2011). These fields then apply an accelerating force to the free electrons, spiralling them away from the galactic core along the length of the rotational axis of the system at relativistic speeds. As they accelerate away outward from the central black hole, they radiate energy. This radiated energy is referred to as synchrotron radiation (Condon & Ransom, 2016). This emission is, of course, non-thermal, as it depends on the magnetic field energy density. The radio sky is dominated by non-thermal radio emitters at the metre and centimetre wavelengths.

The charged particle's centripetal acceleration is what causes the radiation. The spectra of these synchrotron electrons is typically a steep power-law[1]. The radiated power of a single-electron, in the electron gas, is directly proportional to the product of the squares of the electric and magnetic field (Longair, 2011),

$$P_\epsilon = \frac{dE}{dt} \propto E^2 B^2 \,. \tag{1.1}$$

Two things are obvious from Eq. 1.1,

1. Increasing the strength of the magnetic field causes the charged particles to lose energy more rapidly.
2. A higher energy electron loses energy at a higher rate.

Thus, depending on the morphology of the galaxy we can chart the age of the plasma. In the case of FR-II galaxies, fresh plasma can be seen further out due to the plasma that has been dispelled at high relativistic speeds. In FR-I, galaxies older plasma tends to be at larger distances from the radio core due to lower velocity plasma.

The spectrum of a single-electron radiating is pictured in Fig. 1.4, inset plot in the top right corner. For an ensemble of electrons with a similar energy distribution, the synchrotron spectrum would be the same (Rybicki & Lightman, 1986), however, in

---

[1] Where steep is typically $\alpha \geq 1$ in $S_\nu = \nu^{-\alpha}$

reality, electrons have a continuous range of energies and the spectra can be modelled by a power-law.

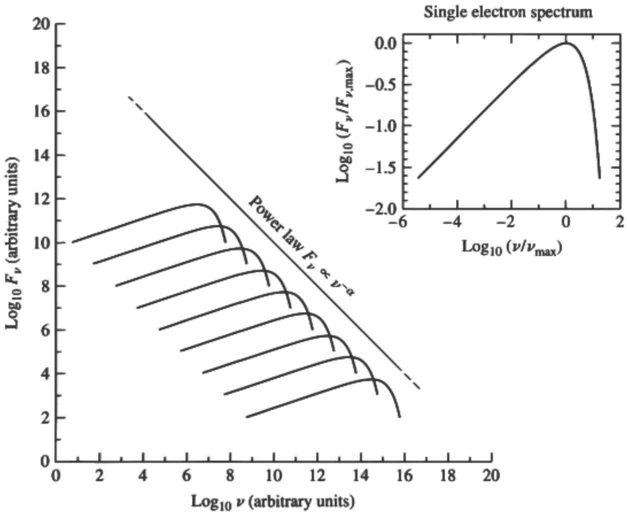

FIGURE 1.4: The synchrotron radiation spectrum of many single-electron spectra (Ertley, 2014).

In addition to Eq. 1.1, increasing the number of particles in any localised region does tend to increase the power of the said region. The number of particles is often modelled as a density, as follows,

$$N(\gamma) \propto \gamma^{-\beta}, \text{where } \beta \approx 5/2, \tag{1.2}$$

where γ is the Lorentz factor. The Lorentz factor defines how much, for an object in motion, measurements of physical properties, such as time, length, and other physical properties change, and it is given by,

$$\gamma = 1/\sqrt{1 - \frac{v^2}{c^2}}. \tag{1.3}$$

For a source with an arbitrary distribution of energetic electrons, the frequency spectrum is a superposition of spectra from the various particles (Rybicki & Lightman, 1986), i.e. the total power from an ensemble of electrons is proportional to the product of the number density and the single-particle radiation law Eq. 1.1. It follows that,

$$P(\gamma) \propto N(\gamma) P_e(\gamma), \tag{1.4}$$

where we now denote P_ϵ by $\mathrm{P}_e(\gamma)$ and $\mathrm{P}(\gamma)$ now denotes the ensemble power. If we fit a linear model to the range of peaks to the electron energy distributions, it is observed that the synchrotron emission takes a characteristic spectrum, whereby the flux steadily drops with frequency as described by the function,

$$F_\nu \propto \nu^{(1-\beta)/2}, \tag{1.5}$$

where $\alpha = -(1-\beta)/2$. For radio and Seyfert galaxies, on average, the value α is measured is in the range 0.70 to 0.75 (Longair, 2011). The symbol α is commonly referred to as the spectral index.

The spectral index can convey information about the emission mechanism and helps characterise the spectra of continuum radio sources (Condon & Ransom, 2016). Equation 1.5 is a measure of the dependence of the flux density F_ν on frequency ν. Spectral indices of thermal and non-thermal sources usually differ, we expect $\alpha \approx -2$ for thermal emission in the Rayleigh–Jeans approximation.

1.2.2 Energy Requirements of a Synchrotron Source

Luminosity depends both on the pervading magnetic field and the particle energy densities[2]. Relativistic protons are, however, also present in this cosmic plasma and we cannot generalise the electron-proton energy distributions, since they vary from source to source. Therefore, to account for the proton energies, we assume that they have energy β times that of the electrons, that is,

$$\epsilon_{\mathrm{p}} = \beta\epsilon_{\mathrm{e}}\,;\ \epsilon_{\mathrm{total}} = (1+\beta)\epsilon_{\mathrm{e}} = \eta\epsilon_{\mathrm{e}}. \tag{1.6}$$

For a radio source the total synchrotron energy is

$$W = G(\alpha)\eta F_\nu B^{-\frac{3}{2}} + V\frac{B^2}{2\mu_0} \tag{1.7}$$

where G(α) is a constant which depends weakly on the spectral index and frequency, μ_0 is the vacuum permeability and V is the volume occupied by the synchrotron emission. Thus from Eq. 1.7 it is clear that the total energy can be inferred from the flux density and the magnetic field strength.

The radio flux depends on the magnetic field strength and the number density of electrons. However, radio observations by themselves cannot distinguish the primary contributing factor between the two and X-ray observations are additionally required for separating the contributions of magnetic field strength and electron density to the radio synchrotron flux (Condon & Ransom, 2016). The total energy has a minimum at some value of the magnetic field, which is approximately equal to the equipartition energy between the electrons and the magnetic field. Fig. 1.5 illustrates this discussion (Longair, 2011).

---

[2] The amount of energy the particles have per unit volume.

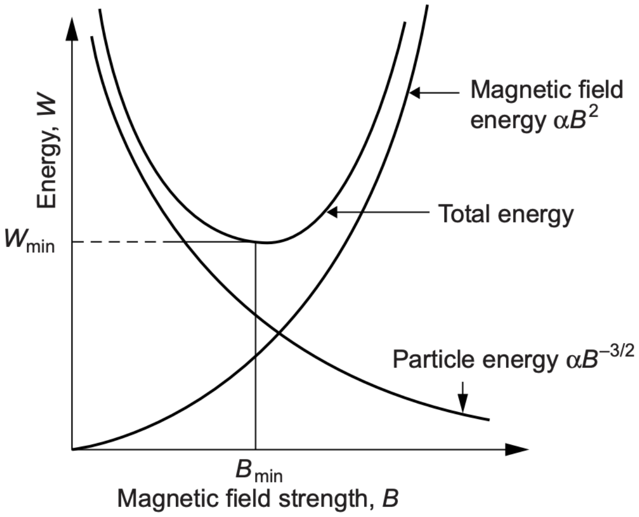

FIGURE 1.5: The minimum-energy requirements of a radio source as a function of the magnetic field strength. The equipartition energy is found at the field strength where the two curves intersect, notice that it is approximately equal to the $B_{\rm min}$. (Longair, 2011).

This minimum total energy is found by minimising the magnetic field,

$$B_{\rm min} = \left[\frac{3\mu_0}{2}\frac{G(\alpha)\eta F_\nu}{V}\right]^{2/7}, \tag{1.8}$$

where all variables have been previously defined. Thus, the minimum-energy requirement becomes,

$$W_{\rm total}({\rm min}) = \frac{7}{6\mu_0}V^{3/7}\left[\frac{3\mu_0}{2}\frac{G(\alpha)\eta F_\nu}{V}\right]^{4/7}. \tag{1.9}$$

The computation of $G(\alpha)$ is complicated so simplifying assumptions are necessary. For a given flux, F_ν, and spectral index, α we can take the frequency limit in evaluating $G(\alpha)$. Thus, we obtain,

$$W_{\rm (min)} \approx 3.0\times 10^6 \eta^{4/7}V^{3/7}F_\nu^{4/7}\nu^{2/7}, \tag{1.10}$$

where V is the volume of the source, measured in cubic meters (m^3), the flux F_ν is in W Hz^{-1} and the frequency ν is in Hz. Refer to Longair (2011) for a thorough derivation. The corresponding minimum magnetic field, in units of Telsa, is,

$$B_{\rm min} = 1.8\left(\frac{\eta F_\nu}{V}\right)^{2/7}\nu^{1/7}. \tag{1.11}$$

Whenever we observe a synchrotron source, we know that relativistic electrons with a magnetic field B and the energy density U_e, with an energy density of $U_B{=}B^2/8\pi$ are the primary factors responsible for the radiation (Longair, 2011).

minimum-energy requirements: ad hoc method

In practice, we do not necessarily know the volume of a radio source, so approximations must be made from the 2D projection of the radio source. The particles and field have a minimum total energy that is required to produce the synchrotron emission with a given luminosity L. The energy density of relativistic electrons is a function of the number of particles within a given energy range,

$$U_e = \int_{E_{min}}^{E_{max}} En(E)\,dE, \tag{1.12}$$

where $n(E)dE$ is the number density of the electrons in the energy range dE. The particle energies are, in turn, a function of the magnetic field $E \propto B^{-1/2}$. Both the electron and field energy densities are a power law of the magnetic field strength,

$$U_B \propto B^2\,;\, U_e \propto B^{-3/2}. \tag{1.13}$$

Thus, taking the ratio of the energy distribution from all particles present in the plasma (Eq. 1.6), we find that the total energy is the sum of the electron energy and the magnetic field densities,

$$W = \eta U_e + U_B. \tag{1.14}$$

Near equipartition, the point at which $\eta U_e \approx U_B$ (Fig. 1.5), the total energy has a minimum. Solving for Eq. 1.14 is a straightforward but laborious task, fully described in (Pacholczyk, 1970) and (Wilson et al., 2013), amongst others. Thus, the minimum-energy magnetic field is,

$$B_{\mathrm{min}} = (4.5\eta c_{12} S)^{2/7} R^{-6/7} \;\; \text{[Gauss]}, \tag{1.15}$$

where $S = \int_{\nu_{min}}^{\nu_{max}} S_\nu \, d\nu$ is the integrated flux, R is the radius of the source and c_{12} (and c_{13} below) is a function that contains the integration over a given bandwidth and the Gaussian CGS units. The corresponding total energy is,

$$E_{\mathrm{total}} = c_{13} (\eta S)^{4/7} R^{9/7} \;\; \text{[ergs]}. \tag{1.16}$$

It is unclear whether most synchrotron sources are near equipartition, but it is the common assumption since systems with interacting components often tend toward equipartition (Condon & Ransom, 2016).

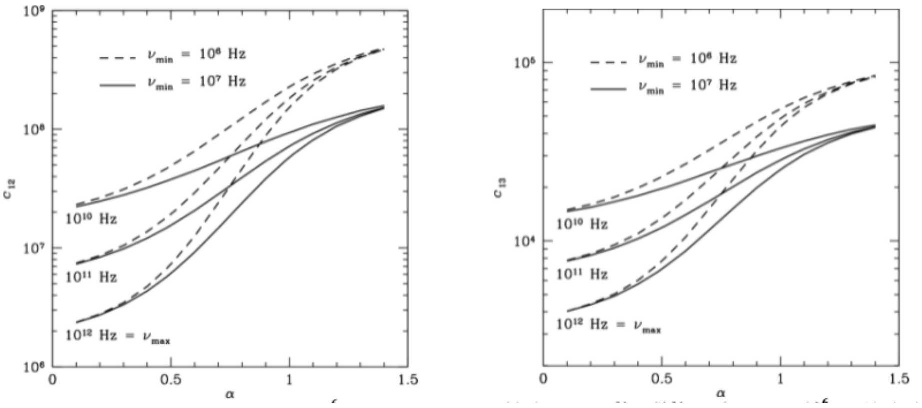

(A) c_{12} (B) c_{13}

FIGURE 1.6: The plots of c_{12} and c_{13} in units of Gaussian CGS as a function of spectral index ($S_\nu \propto \nu^{-\alpha}$). Credit: (Condon & Ransom, 2016).

The parameter η has not been measured for extragalactic radio sources such as M87 and Cygnus A, whose cosmic ray population may primarily be electrons and positrons. Electrons and positrons both have a large charge to mass ratios, so an electron–positron plasma would have an $\eta \approx 1$ (Condon & Ransom, 2016). The proton-electron mass ratio is ~ 2000 and $\eta \sim 2 \times 10^3$. It turns out that $B_{\text{min}} \propto \eta^{2/7}$ is weakly dependent on η, that is varying η from 1 to $2{\times}10^3$ changes $\eta^{2/7}$ from about 1 to 9 (Condon & Ransom, 2016).

1.2.3 Synchrotron Self-Absorption

In an idealised case, the synchrotron radiation emitted by the electrons reaches the observer without any disturbances (absorption or scattering). In reality, if the intensity of synchrotron radiation is sufficient, i.e. when the brightness temperature of the source reaches the equivalent kinetic temperature of the electrons (Kellermann et al., 2007; Longair, 2011), there is a possibility that the photons emitted may scatter off the synchrotron electrons. Should this occur enough times, an observer will only detect emission from a thin layer near the surface of the source (Condon & Ransom, 2016; Longair, 2011).

The flux an observer would see would be magnitudes smaller than if all the synchrotron photons hadn't scattered. The depth at which we see into a source is a function of the frequency observed. We see deeper into a source as our observing frequency increases (Longair, 2011). Regions in which there is self-absorption are those in which the mean free path of a photon is much smaller than the source size[3], regions where scattering occurs. In this case, this region in the plasma would be referred to as being optically thick. Conversely, regions with fewer scattering and thus a longer mean free path are referred to as optically thin (Longair, 2011).

The effects of synchrotron self-absorption are mostly pronounced in sources where inverted spectral indices are as steep as $\alpha = 1$. These spectral indices are typically observed at long wavelengths (Kellermann & Verschuur, 1988).

1.2.4 Spectral Ageing

The varying radio spectra is largely attributed to spectral ageing, the magnetic field and plasma density, and opacity effects. Ageing is a measure used to quantify the age of the seed population and thus also constrains the age or the dynamical history of the source (Jaffe & Perola, 1973; Myers & Spangler, 1985). Oftentimes, spectral ageing is taken to mean that the particle number density varies over the structure of the galaxy. The spectral age of charged particles is thus given by,

$$t_{\text{cool}} = \frac{\sqrt{54\pi m_e c\, eB\nu_{\text{syn}}^{-1}}}{\sigma_T(B_{\text{CMB}}^2 + B^2)}. \tag{1.17}$$

This result is obtained from Pfrommer & Jones (2011). The variables represent the following, c the speed of light, m_e and e are the mass and charge of an electron, B the magnetic field strength of the feature being observed, σ_T is the Thompson cross section, $\nu_{\text{syn}} = (3eB\gamma^2)/(2\pi m_e c)$ is the break frequency and is defined as the frequency at which the electrons of Lorentz factor γ radiate their synchrotron emission and B_{CMB} is the equivalent magnetic field of the CMB due to inverse Compton process and is equivalent to,

$$B_{\text{IC}} = 3.2(1+z)^2\,\mu\text{G}, \tag{1.18}$$

---

[3] The average distance over which a particle in motion changes its energy, typically seen as a result of collisions with other particles.

where z is the redshift. Eq. 1.18 is a result from Govoni & Feretti (2004).

1.2.5 Brightness Temperature

This is an important concept in radio astronomy. It refers to the temperature which a radiating body would be, given its solid angle and flux density, had it been a black-body. It is regardless of the true radiation mechanism of the source. It is the temperature a hypothetical black-body, in the place of the object in observation, would have. The brightness temperature of an object is not the object's temperature in the canonical sense, it is a pseudo temperature, used as a proxy of how intense the radiation is, a measure of the received intensity.

1.3 Radio galaxies in cluster environments

1.3.1 Galaxy clusters

Galaxy clusters are collections of galaxies that are gravitationally bound together. With masses ranging from 10^{14} to 10^{15} $\mathrm{M}_{\odot}$. Galaxy clusters are typically made up of 9% intergalactic gas in the intracluster medium (ICM), with 1% being actual galaxies. The most massive component is dark matter, with a fractional mass of 90%. For instance, the Virgo Cluster's ICM is about 3×10^{14} $\mathrm{M}_{\odot}$, however, the cluster's total mass is about 1.2×10^{15} $\mathrm{M}_{\odot}$ (Fouqué et al., 2001).

1.3.2 Intracluster medium

The ICM is characterised by its metallicity (which is important for star formation), temperature and density. These properties are known to peak in the centres of clusters (Mantz et al., 2017; Peterson & Fabian, 2006).

Clusters are regions of high gas density, with their cores being as dense as $10^{-1}\,\mathrm{cm}^{-3}$[4] in denser clusters and $10^{-3}\,\mathrm{cm}^{-3}$ in the less dense ones. These densities are higher than the mean cosmic density of baryons which is about $10^{-8}\,\mathrm{cm}^{-3}$ (Peterson & Fabian, 2006). Hydrogen and helium are the most abundant elements in the universe and this reflects in the ICM as these account for the majority of the baryonic material in galaxy clusters.

Heavier metals[5] are known to exist in the ICM, with a metallicity of about 0.3–0.5 of the Solar metallicity (Mushotzky et al., 1978). Metallicity is defined as the average amount of heavier elements relative to hydrogen in the ICM. The ICM metallicity is a function of radius from cluster cores, with the cores having a higher metallicity than the outer regions (Mantz et al., 2017).

The structure of the ICM can be approached from two perspectives, first the ionised plasma and second the radiation emission processes. The ICM generates an enormous amount of energy in the form of X-rays with an average temperature of 10^{6-8} K (Sarazin, 1986). This radiation is mainly through thermal bremsstrahlung processes. Two things are of note, this allows for the observation of the ICM by detecting these X-rays and the emission of these X-rays will lower the temperature of the plasma, since

---

[4] We quote the number densities and not mass densities.

[5] These metals (any element that is heavier than helium) are almost exclusively made in stars and ejected from galaxies into the ICM through processes such as supernova explosions and AGN outflows.

energy is carried away by the X-rays as they leave the cluster (Peterson & Fabian, 2006).

1.3.3 Cooling Core Galaxies

In the central regions, the ICM density is at its highest, it follows that the radiative cooling time (Eq 1.17) is shorter, as governed by Eq 1.4. When enough energy is radiated, the central cooled gas can no longer support the weight of the external hot gas and a cooling flow results, in a process whereby the hot gas from the external regions gradually flows towards the centre of the cluster (Fabian, 1994).

If the mass ratio (the ratio of the more massive sub-cluster to the mass of the least massive sub-cluster) is large (~ 10) cold fronts may develop in cooling core clusters due to "sloshing" induced by the in-falling of one galaxy through another (Markevitch & Vikhlinin, 2007). Cold fronts are defined as sharp contact discontinuities at the interface between gas regions with different temperatures and densities, like the interface between the ICM and synchrotron electrons emerging from a galaxy (Ascasibar & Markevitch, 2006). Cold fronts differ from shocks in that should features A and B have been shocks, the gas on the denser, in-falling side would have to be hotter than that on the less dense, out-flowing side (Markevitch & Vikhlinin, 2007).

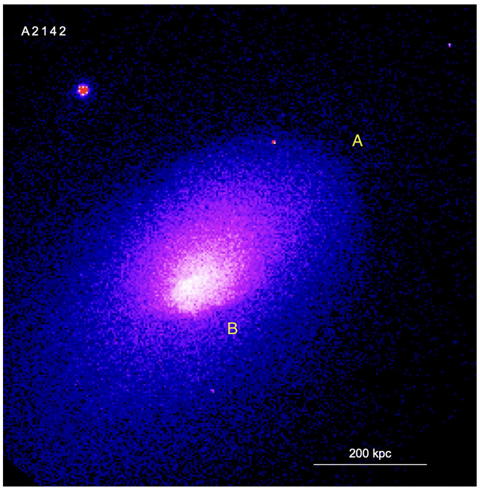

FIGURE 1.7: One of the first Chandra X-ray images of clusters with cold fronts, A2142. Sharp brightness edges are seen, at structures labelled A and B. Image credit: (Markevitch & Vikhlinin, 2007).

1.4 M87

1.4.1 Overview of its physical properties

M87 is a giant elliptical galaxy near the dense environment of the centre of the Virgo cluster. It is known by many other names, Virgo A and 3C 274 being the names of the radio source associated with M87 and NGC 4486, the names for the host galaxy. Owing to its rich history, M87 has been imaged at virtually every scale that is achievable with modern technology. Down at a few Schwarzchild radii we have the black hole shadow of M87, imaged by The Event Horizon Telescope Collaboration (Event Horizon Telescope Collaboration et al., 2019a). Up at ~ 100 kpc scales, we have large radio halos as imaged by connected arrays like the VLA (Owen et al., 2000) and LOFAR (de Gasperin et al., 2012).

Mass constraints have been placed on the SMBH that powers the galaxy, using gas dynamics is $M = 3.5 \pm 0.4 \times 10^9$ $M_\odot$ (Walsh et al., 2013) and stellar dynamics 6.6 $\pm 0.4 \times 10^9$ $M_\odot$ (Gebhardt & Thomas, 2009). At this distance, 1 arcsec ≈ 89 pc. The radio structure is ∼ 15 arcmin (80 kpc) in scale. M87 lies within a typical "cooling flow" cluster. It has highly collimated jets, which can be observed in radio, optical and X-ray wavelengths and due to relativistic beaming the jet that points northwesterly is more prominent. M87 has been the subject of study of many papers for two main reasons: it is very close to us and it is one of the brightest radio sources in the sky (de Gasperin et al., 2012).

TABLE 1.1: Some M87 physical properties. The luminosity was obtained from (Herbig & Readhead, 1992) in the frequency range 10 MHz to 150 GHz, scaled to 17 Mpc.

Redshift	0.004
Projected size	150 kpc
Distance	17.9 Mpc
black hole mass	$3.5 - 6.6\,M_\odot$
Core radio power	9.6×10^{34} W
Jet power	$\sim2.8\times10^{35}$ W
Total Radio Power	$\sim9.6\times10^{34}$ W
Core position (J2000)	RA 12:30:49.40 Dec +12.23.28.00

In this introduction, we have covered several astrophysical concepts that are relevant to understanding M87's morphology, from sub- to mega-parsec scales. A summary is that M87 is a giant elliptical galaxy, powered by a radio loud AGN, it resides in the dense environment of the centre of a cooling flow cluster. Due to this, it has an amorphous morphology at scales that are large enough to interact with the ICM. At smaller scales, it exhibits the FR-II structure of dual jets that terminate with hotspots.

In the next two sections, we show two papers that are key to our study (de Gasperin et al., 2012; Owen et al., 2000). Owen et al. (2000) reviews the work on M87 undertaken over the decades and presents the first large scale image of M87 in radio wavelengths. de Gasperin et al. (2012) builds on this work at lower frequencies and does an extensive spectral index study on the M87 halo.

1.4.2 VLA 327 MHz observation of M87: a brief review

As will become apparent, the MeerKAT observations are best compared with the VLA 327 MHz from Owen et al. (2000). Given its importance, we provide a detailed review of the Owen et al. (2000) results. Some notable work published over the last 20 years includes the large-scale, low-frequency LOFAR perspective of M 87 at metre wavelengths (de Gasperin et al., 2012), of which we shall, also, review at length in the following section.

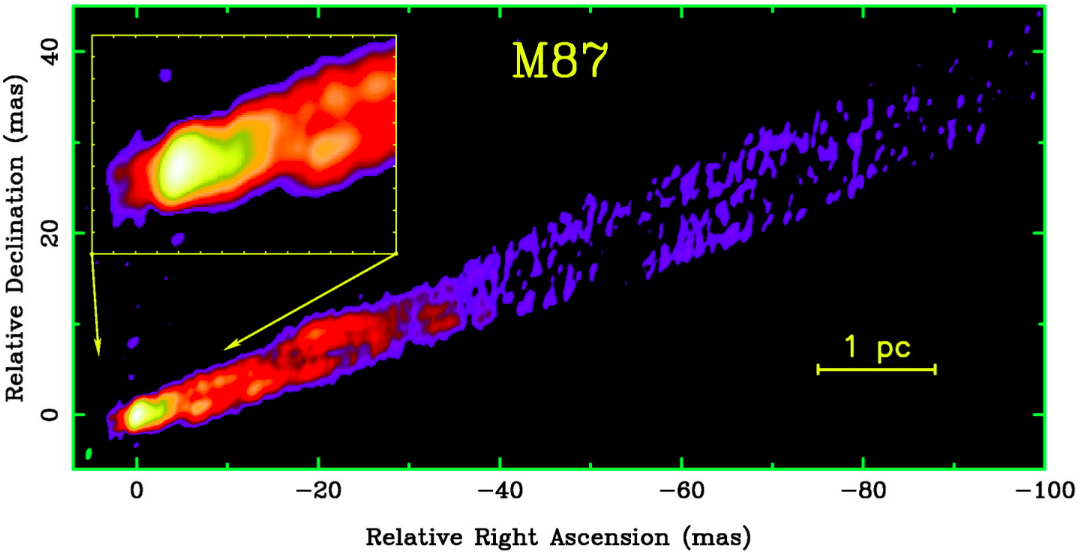

FIGURE 1.8: A VLBA 2 cm image of the M87 jet. A beam of 0.6 x 1.3 mas, B.P.A. = -11 deg. The peak intensity is 1.00 Jy beam^{-1}, rms noise 64 µJy beam^{-1}. Credit: (Kovalev et al., 2007).

VLA

The **V**ery **L**arge **A**rray (VLA) is a centimetre wavelength telescope in central New Mexico, USA, composed of 27 × 25 metre parabolic dish antennas, plus an additional dish which substitutes for maintenance. The antennas are mounted on rails, which allows for 4 baseline configurations A, B, C and D. The A-configuration has the longest maximum baseline of 36 km and D brings all the antennas within 1 km. The angular resolution ranges between 1 arcsec (A-config) to ∼ 45 arcsec (D-config), at L-band frequencies. Each antenna is fitted with 10 receivers (74 and 327 MHz, 1.4, 3, 5, 8.4, 15, 22, 33, 43 GHz)

FIGURE 1.9: The VLA antenna layout. The antennas are arranged in a Y configuration to allow for a variety of reasons, as explained in the text. Credit: NRAO.

The benefits of having a Y-configuration are, in addition to the ability to change baseline lengths with three rails. This produces a nearly circular synthesized beam for various integration times and most positions in the sky. It is an optimal arrangement, for connecting the antennas to a central power and communication centre. Amongst other things, the VLA is suited for imaging diffuse large-scale emission, such as that of M87.

Methodology

For cross-calibration, Owen et al. (2000) used the calibrator 3C 286, which doubled as an amplitude and phase calibrator. Their flux density scale was derived from Baars et al. (1977). They imaged using the AIPS IMAGR in 3D mode and performed selfcal using `CALIB`. Confusing sources were subtracted from the visibilities, then imaging and calibration were performed on just the target field containing M87. The final map was created using the maximum entropy program VTESS. A more detailed comparison of bandwidth, sensitivity and resolution are discussed in Chapter 3.

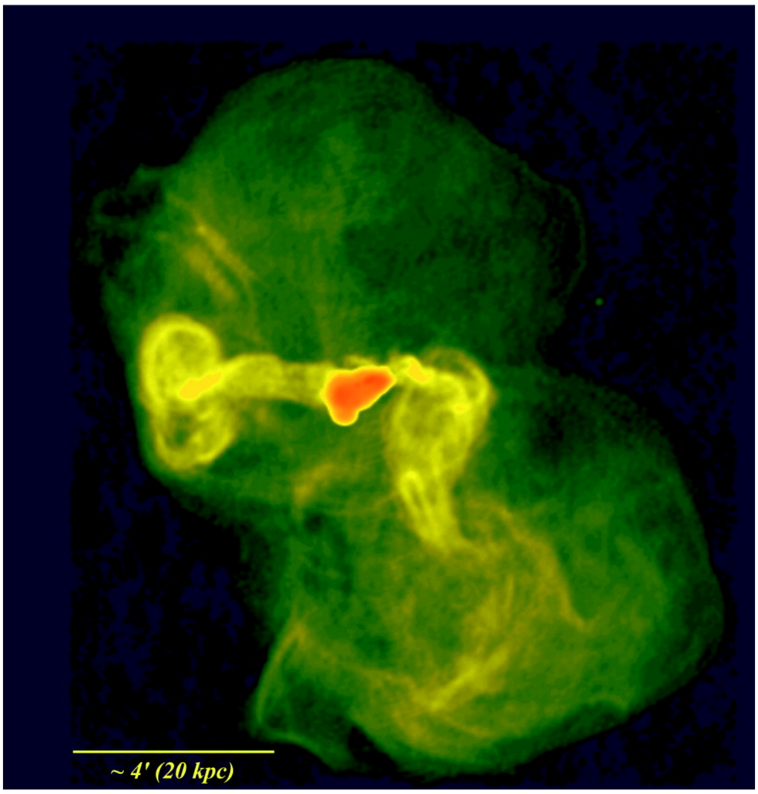

FIGURE 1.10: The VLA view of the M87 radio halo at 327 MHz. The maximum entropy convolving beam is 7.8×6.2 arcsec, $BPA = 86$ deg. Imaged with the maximum entropy based, `AIPS` software, `VTESS`. Residuals are not added back into the final image (Owen et al., 2000).

Results

The Owen et al. (2000) observations revealed the M87 halo for the first time and brought out its prominent features, which include a limb-brightened edge and filamentary features that fill the southern region of the halo (Fig. 1.11). Their work performed some of the first astrophysical calculations on the halo, i.e., minimum pressure calculations at the various zones labelled in Fig. 1.11. Structure B in Fig. 1.11 is argued to be in a turbulent flow as it seems that the gas has formed a subsonic vortex ring (Owen et al., 2000).

Structure A seems to extend further beyond the sharply defined halo edge. This is coincident with the X-ray cavity discovered in Forman et al. (2007).

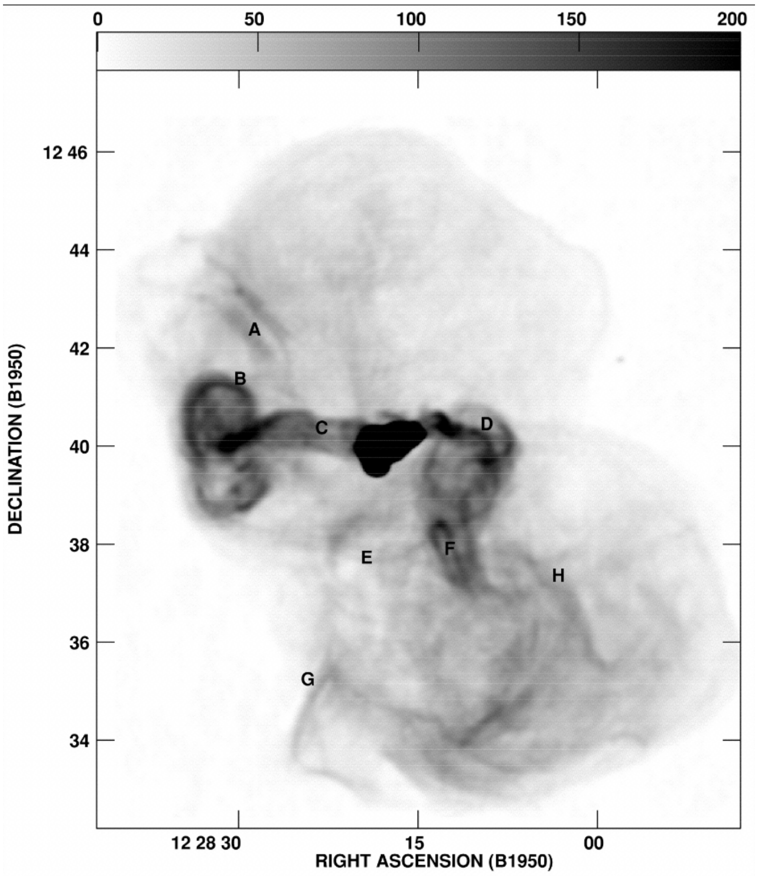

FIGURE 1.11: A grey-scale map of M87 showing regions of minimum pressure (Owen et al., 2000).

Fig. 1.12, taken from Forman et al. (2007), is a *Chandra* ACIS-I observation of M87 imaged at energies within the range $0.5 - 2.5$ keV. What is interesting is the fact that the outer cavity, as labelled in the figure, coincides with the VLA 90 cm map. The outer X-ray cavity coincides with the radio emission that extends beyond the halo edge. The outer ring is further down from the edge of the radio emission (Forman et al., 2007).

It has been demonstrated that there is an anti-correlation between X-ray- and radio-emission in nearby clusters, implying mechanical feedback by the large-scale jets (Churazov et al., 2000; Bohringer et al., 1995a; McNamara & O'Connell, 1993; Fabian et al., 2000). Contrary to this, a comparison of radio to X-ray images (Fig. 1.12) shows that the radio and X-ray emission correlate strongly near the core of the M87 (Owen et al., 2000). This, makes M87 a very interesting galaxy, potentially in an earlier stage of the onset of the jet-driven feedback. We will revisit this phenomenon, in more detail, in Chap 3.2.

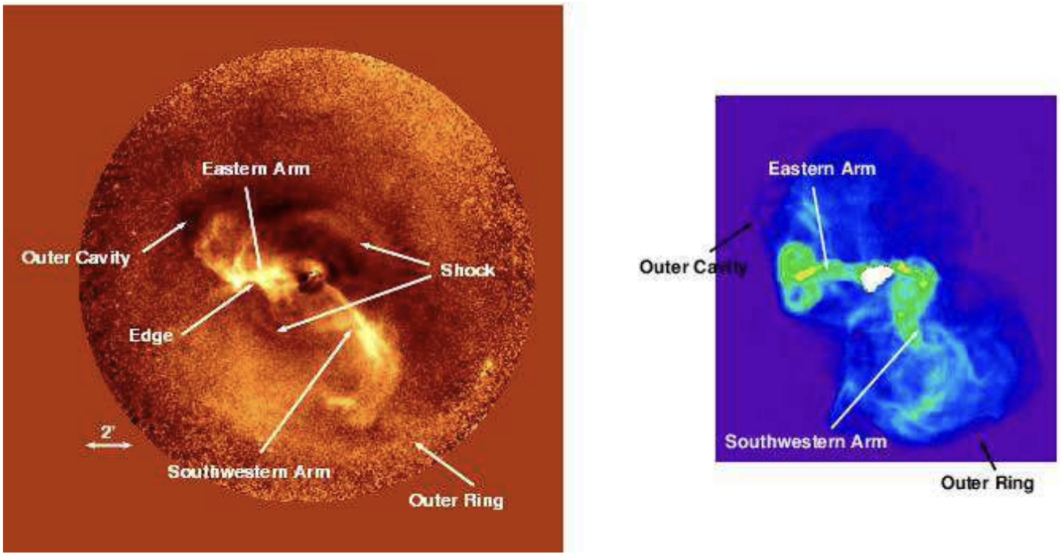

Figure 1.12: X-ray and radio views of M87, as imaged by Chandra and VLA 327 MHz, respectively. The images are set to the same scale. The eastern and southern regions are seen in both the X-ray and radio. Chandra image credit (Forman et al., 2007), VLA credit (Owen et al., 2000).

Conclusions

Owen et al. (2000) concluded that M87 is an active galaxy, in contrast to what was initially thought about M87, that it is a relic of previous activity (Turland & Scheuer, 1975). The hot ICM gas seems to be strongly interacting with the jets and lobes. In addition, it has been shown that the energy input into the region from the M87 core is greater than the energy that is being radiated. They continue to argue that the AGN and the cluster's cooling core are at a "tug of war". The AGN works against the cluster's cooling inputting energy into M87's halo and thus into the cluster, whilst the cluster is radiating energy away in the form of X-rays, thus resulting in a cool core.

However, even though the AGN is radiating strongly at the time being, they suggest that it is transient, i.e. occurring on a relatively short time scale. It has been demonstrated that galaxies that sit at the cores of cooling clusters have gone through heating/cooling cycles in their lifetimes. If the AGN activity ceases or slows, the cooling flow process will then dominate, perhaps M87 has, itself, gone through these cycles over its lifetime.

1.4.3 LOFAR 140 MHz observation of M87: a brief review

Being a low-frequency successor to Owen et al. (2000), de Gasperin et al. (2012) does a follow up study on M87, some 12 years later. The paper presents M87 images at low frequencies (20-140 MHz) that have never been explored at this high dynamic range and spatial resolution. The study delves into an in-depth spectral analysis and places constraints on the magnetic field, age and energetics of M87. The study makes use of a 10.55 GHz Effelsberg map and VLA archival images at 325, 1400 and 1600 MHz.

LOFAR

LOw **F**requency **AR**ray (LOFAR) is an international telescope that spans several European countries[6], comprising 51 stations. It is operated by ASTRON, the Netherlands Institute for Radio Astronomy. Two types of antennas are present at each station, the **H**igh **B**and **A**ntennas (HBA), which operate in the frequency range 110-240 MHz) and the **L**ow **B**and **A**ntennas (LBA), in the range 10-90 MHz. LOFAR is an interferometric array of 8000 dipole antenna stations spread across the Netherlands and Europe (van Haarlem et al., 2013).

FIGURE 1.13: The LOFAR core. In the upper right and lower left of corners of the three additional LOFAR cores stations can be seen. Each of these core stations includes a field of 96 LBAs and two sub-stations of 24 HBAs each (van Haarlem et al., 2013).

LOFAR's dipole stations have no moving parts, but with the aid of software the array, effectively, has an all-sky **F**ield **o**f View (FoV), in principle. In reality, stations are phases up, thus reducing the FoV. The core hosts 24 stations within a 2 km radius. The core is $\sim$30km from Dwingeloo, NL (van Haarlem et al., 2013). The receivers have different designs, the LBAs are inverted-V crossed-dipoles oriented NE-SW and SE-NW, while the HBA are organized into tiles made of a 4×4 array of bow-tie-shaped crossed dipoles. The array can "point" in different directions by applying different phase delays to the incoming signal (de Gasperin et al., 2012).

---

[6] Netherlands, France, Germany, Ireland, Latvia, Poland, Sweden and the UK.

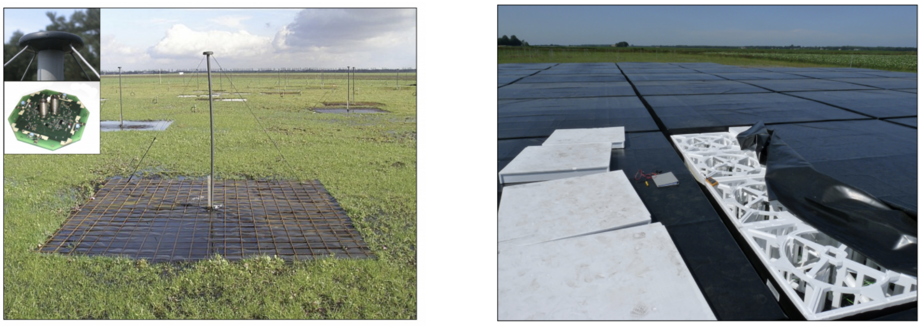

(A) (B)

FIGURE 1.14: LOFAR receiver types. Left: a single LBA dipole including the ground plane. The insert images show the moulded cap containing various electronics. Right: a single HBA tile, where the covering has been partially removed to expose the dipole assembly. The circular dipole rotation mechanism is visible (van Haarlem et al., 2013).

Methodology

de Gasperin et al. (2012) presents a set of three observations, at 15-30 MHz (LBA-low), 30-77 MHz (LBA-high) and 116-162 MHz (HBA), made during the commissioning phase of LOFAR. Each observation has a duration of 8 hours and all polarisation products were recorded. Within these observations, the channel width were further divided into sub-bands of channel width 0.1953 MHz and each sub-band was subsequently divided into 64 channels of channel width 3 kHz.

The LBA visibility data had an integration time of 1 second, while the HBA visibilities were sampled every 2 seconds. The data calibration was performed with the use of pipeline software. For an exhaustive description of the software, we refer you to Heald et al. (2010). The various sub-bands follow different calibration schemes, with some common steps. Using `AOFlagger` (Offringa, A. R. et al., 2012), initial flagging is performed in time and frequency on the full resolution data. The data was then inspected for any visible RFI.

From there onward, the procedures followed different calibration schemes. Then after the data was averaged to one channel per sub-band and to 20 seconds of sampling time. The self-calibration model was obtained from the 325 MHz, 7 arcsec resolution (Owen et al., 2000) data set. In order to converge on the final image, several selfcal-imaging rounds were performed with BBS and the `CASA` task `CLEAN`, respectively.

The LBA-high sub-band also went through a demixing procedure, similarly to the HBA. Then, the data was compressed to one channel per sub-band and to a 10 seconds integration time. Here the self-calibration model was extracted from a VLA observation at 74 MHz (Kassim et al., 1993). Several cycles of amplitude and phase self-calibration were performed with BBS and imaging was performed, again, using `CLEAN`. The central region was deconvolved using typical pixel-by-pixel cleaning, while the extended emission was multi-scale `CLEAN`ed.

Results

Below (Fig. 1.15), we show the LOFAR HBA M87 image at 140 MHz. `CASA` was used, with the multi-scale deconvolution algorithm, to image the entire 48 MHz. A Briggs weighting of `robust` = `−0.5` was used.

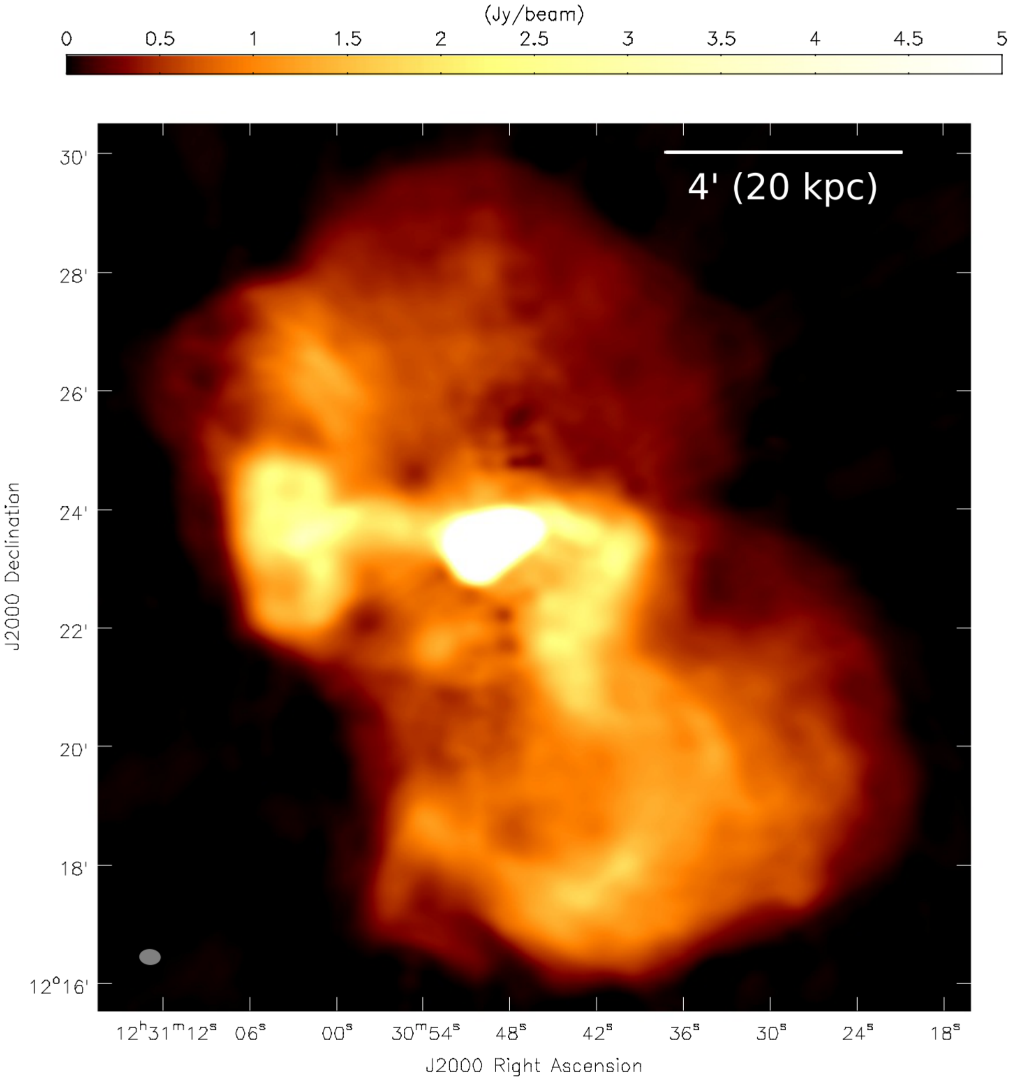

FIGURE 1.15: The LOFAR-HBA (140 MHz) image of M87. The rms-noise level is $\sigma = 20\,\mathrm{mJybeam}^{-1}$, the flux peaks at 101 Jy beam^{-1} and the restoring beam size is 21×15 arcsec (shown bottom left). Deconvolution bowls are seen as small patches just above and below the core. Fig. 5 of de Gasperin et al. (2012).

In Fig. 1.16, 4 LOFAR-LBA images are shown. Each image is produced with `CASA` using a multi-scale multi-frequency deconvolution algorithm (Cornwell, 2008; Rau & Cornwell, 2011) on a subset of 60 sub-bands with uniform weighting.

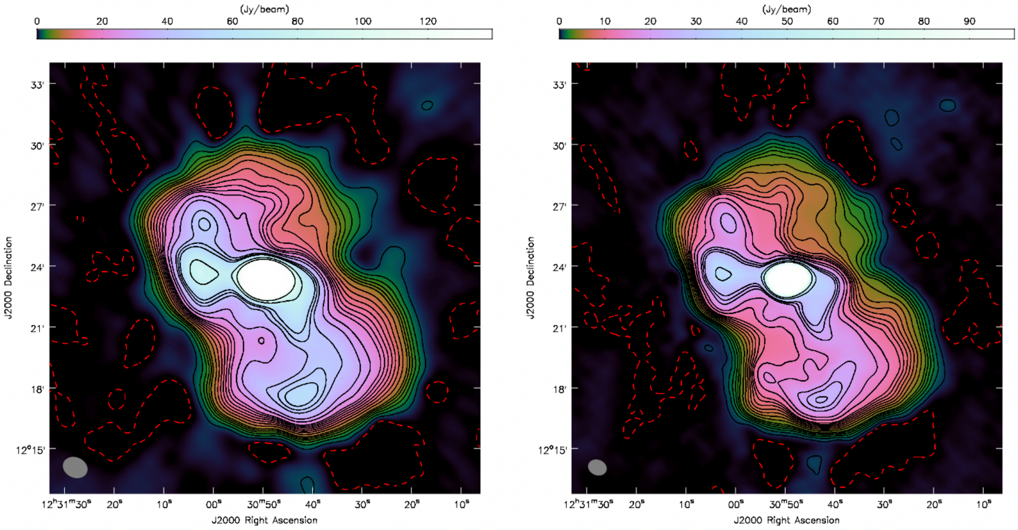

(a) 36 MHz – RMS: 0.2 Jy/beam – Beam: 73″ × 58″ (b) 48 MHz – RMS: 0.09 Jy/beam – Beam: 55″ × 43″

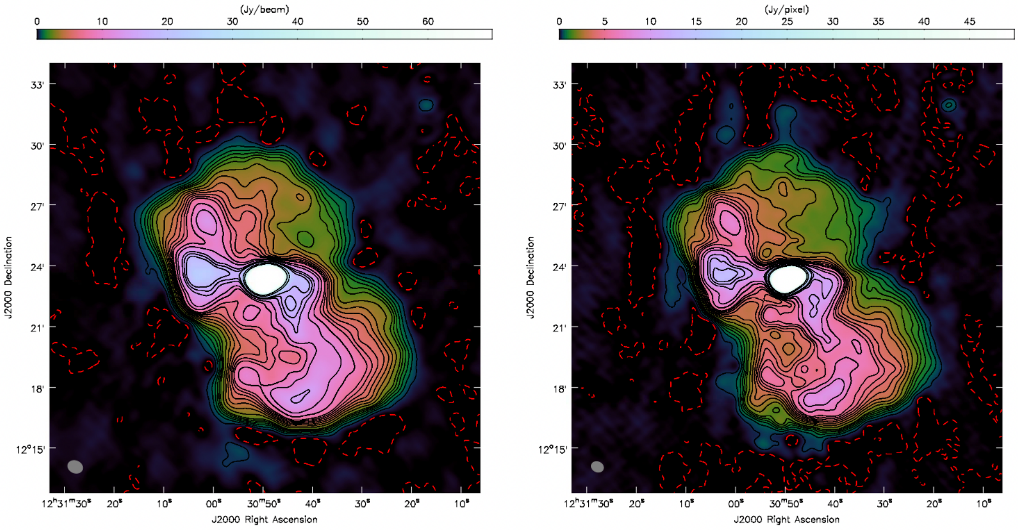

(c) 59 MHz – RMS: 0.07 Jy/beam – Beam: 45″ × 36″ (d) 71 MHz – RMS: 0.05 Jy/beam – Beam: 37″ × 30″

Figure 1.16: LOFAR-LBA images of M87 within the frequency range 36-71 MHz. The images are a result of a multi-scale multi-frequency cleaning on a subset of 60 sub-bands. Positive contours are shown as black lines at (1, 2, 3, 4, 5, 6, 8, 10, 12, 14, 16, 18, 20, 25, 30, 25, 40, 45, 50, 75, 100) $\times 5\sigma$. Negative contours at -1σ are shown as red dashed lines. Fig. 6 of de Gasperin et al. (2012).

Finally, Fig. 1.17 is the 25 MHz image of M87. Through the use of `CASA` the image was made with uniform weighting. Multi-frequency deconvolution and multi-scale modes were enabled.

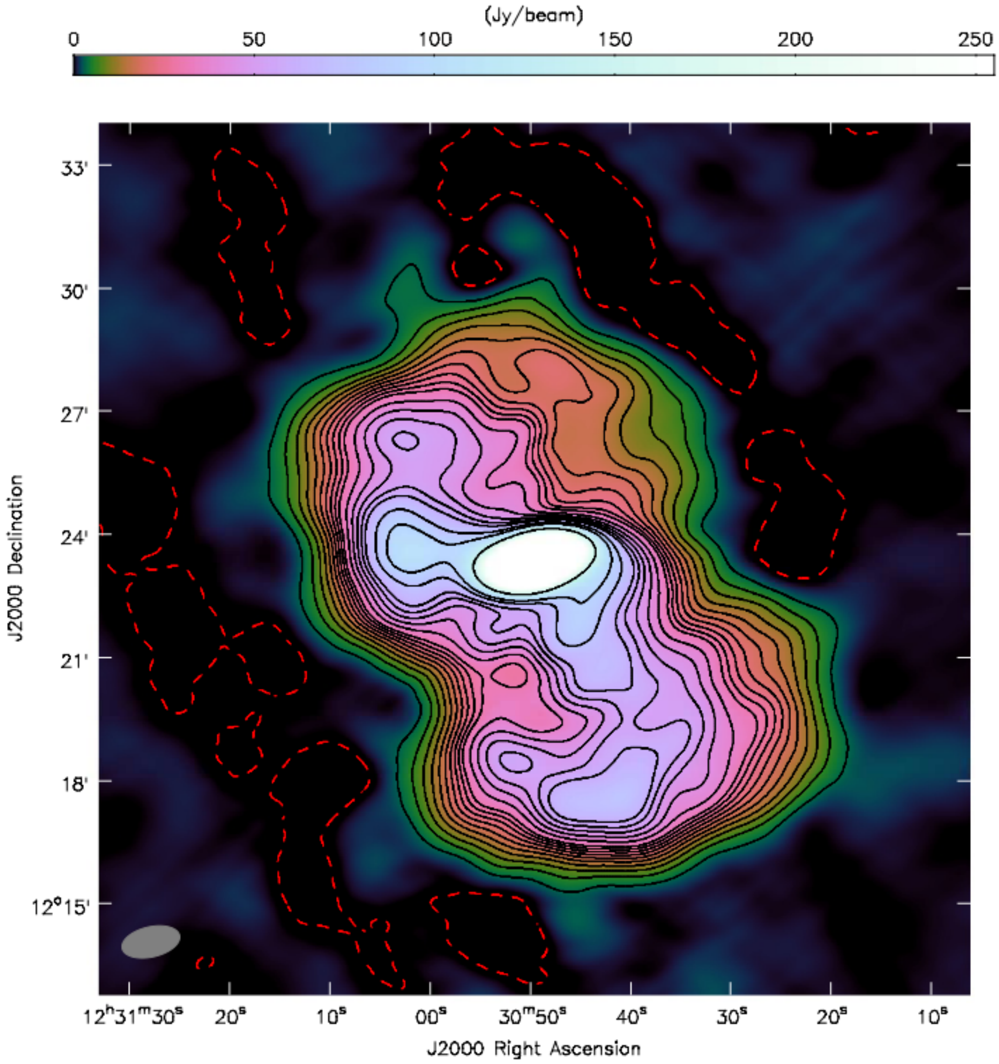

FIGURE 1.17: The LOFAR 25 MHz image of M87. The rms-noise sits at $\sigma = 0.6$ Jybeam^{-1} and the beam size is 85 arcsec ×44 arcsec. Positive contour levels are represented by black lines at (1, 2, 3, 4, 5, 6, 8, 10, 12, 14, 16, 18, 20, 25, 30, 25, 40, 45, 50, 75, 100) $\times 5\sigma$. Negative contour levels at -1σ are represented by a red dashed line. Fig 7. of de Gasperin et al. (2012).

Spectral index map

In making their spectral index map (de Gasperin et al., 2012) excluded the low-frequency part of their LBA data, so that the angular resolution could be kept at 50 arcsec. All LBA and HBA images, from all sub-bands, were convolved to 50 arcsec, then averaged such that there was only one image in the LBA frequency range and one in the HBA frequency range. In Fig 1.18 we show the low-frequency spectral index map, which was created by applying a linear regression model to each pixel from the LOFAR-HBA (115-162 MHz), the LOFAR-LBA (45-77 MHz) and a VLA (325 MHz observation.

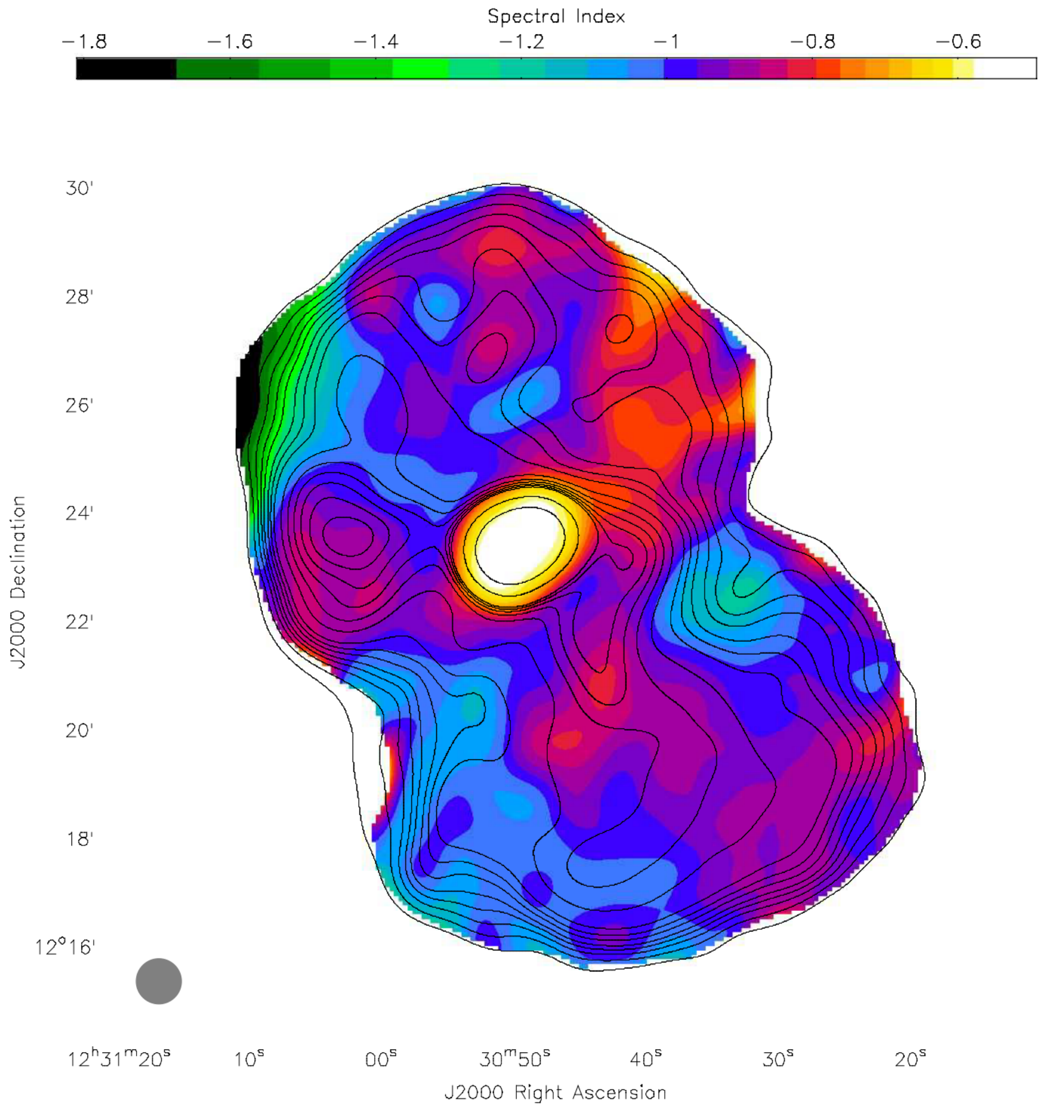

FIGURE 1.18: The LOFAR M87 spectral index map. This was obtained from LOFAR LBA in the range 45-71 MHz and LOFAR HBA in the range 115-162 MHz, this also makes use of the VLA map at 325 MHz. All maps were convolved to a resolution of 50 arcsec. The image was made by pixel-by-pixel linear regression was model. Contours are generated from the 325 MHz map. (de Gasperin et al., 2012).

Using the convention of a negative α ($S_\nu \propto \nu^\alpha$), the core has a reported spectral index ranging from -0.55 to -0.6. The spectrum follows a power law down to 30 MHz.No apparent self-absorption was observed down to these frequencies (30 MHz).

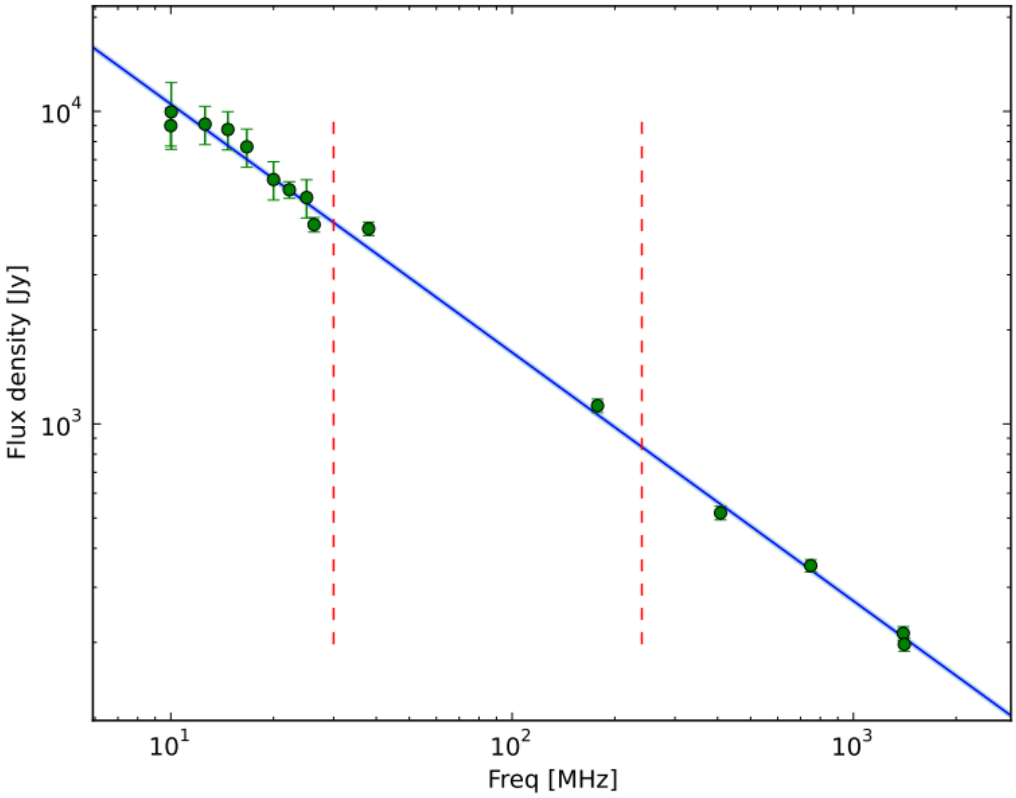

Figure 1.19: The integrated flux of M87 at the various frequencies obtained from archival data. A linear fit slope of -0.79 is fit to the data. The two dashed lines indicate the boundaries of the LOFAR data. (de Gasperin et al., 2012).

The spectral index flattens by 10-20% in the southern lobe, where the bright flow twists and bends. Similar results are seen in the eastern lobe. It is noted that it could be due to the low resolution of the spectral index map. There is a faint extension towards the northeast of the boundary, this is the steepest part of the halo (spectral index of 1.8). This region is coincident with what Forman et al. (2007) establish as an external cavity in the X-ray halo.

Conclusions

Building on the work undertaken by Owen et al. (2000), de Gasperin et al. (2012) also concluded that the M87 halo is active and not a relic of past activities. Even at these lower frequencies (15-162 MHz) no previously undetected steep spectrum features were discovered. An average magnetic field of 13 μG, 10 μG and 30 μG were found in the outflows, halo and core regions, respectively (de Gasperin et al., 2012). Their minimum pressure estimates reveal that the plasma and magnetic field pressure alone cannot sustain the halo against external pressure and thermal gas is also probably playing a role in sustaining the halo. They, however, also note that some of the assumptions they made may not be correct, i.e. they assume that there is a continuous supply of particles from the central source based on the Pacholczyk (1970) model.

1.5 Thesis objectives and outline

M87 is an important source for several reasons, its proximity to the nearby universe and its high luminosity. Due to these, it has been the subject of many studies that attempt to further our understanding of radio galaxies and the influence they have on their immediate environments. As is often done, we revisit this well-studied source with the new capabilities of MeerKAT, which is ideally suited to image complex sources with diffuse, low surface brightness features.

Our main intentions are to, first, generate a MeerKAT full-channel width map of M87, and second, to perform a quantitative study on its extended structure, i.e. radio lobes and halo. A comparison follows naturally, between our maps of the M87 large-scale structure, the de Gasperin et al. (2012) and Owen et al. (2000) maps. One of our primary aims is to validate the complex morphology uncovered by the VLA 327 MHz map, which was produced with a maximum entropy imaging algorithm.

The merit of the project is in probing the electron cooling history, by measuring the spectral index in the outer, diffuse emission in the map. MeerKAT's wide-band, high sensitivity, and imaging fidelity are key, in order to perform an in-band spectral index map. We aim to connect the small-scale features of the galaxy to the outermost lobes and halo in order to fully account for the energy output.

The structure of the dissertation is as follows. Following this chapter's introductory overview, we present the methodologies used in our data processing and analysis in Chapter 2, Chapter 3 delves into our findings and Chapter 4 summarises the work and outlines future work.

Chapter 2

Observations, calibration and imaging

2.1 MeerKAT: an overview

MeerKAT is a 64-antenna telescope in the Karoo, within the Northern Cape province of South Africa. It is a precursor for the SKA-mid array. Each of the 64 antennas is an offset Gregorian, 13.5 m diameter dish. The antenna configuration follows a "pinched core" layout, where 70% of the antennas, as seen in Fig. 2.2, are within a half-kilometer radius, are laid out in a 300 m σ two-dimensional Gaussian distribution of a minimum baseline of length of 29 m and a maximum baseline length of 1 km. The remaining 30% of the collecting area, pictured in Fig. 2.3, scattered over a 4 km radius with a maximum baseline length of 8 km, are also in a two-dimensional Gaussian distribution with a larger σ of 2500 m (Jonas, 2009)[1].

MeerKAT uses an FX-type correlator. It first performs a Fourier transform (F) to frequency is performed,then a cross-correlation (X) follows and it has two main channelisation modes, a wide-band coarse mode (4K mode) where the number of channels is 4096 and the bandwidth is 209 kHz and a wide-band fine mode (32K mode), comprising of 32768 channels and a 26 kHz bandwidth (Jonas, 2009).

MeerKAT has two observational frequency bands in operation, L-band (856-1712 MHz) and UHF (544 to 1088 MHz), with S-band (1.8-3.5 GHz) still to be commissioned. At L-band the MeerKAT maximum attainable angular resolution is approximately 5.4 arcsec. In Fig. 2.1 we show a photograph of some of the core region antennas of MeerKAT.

FIGURE 2.1: A subset of the MeerKAT array, near the core. Credit: SARAO.

---

[1] Some of the information in this section was obtained from `https://skaafrica.atlassian.net/servicedesk/customer/portal/1/topic/bc9d6ad2-8321-4e13-a97a-d19d6d019a1c/article/315621435`

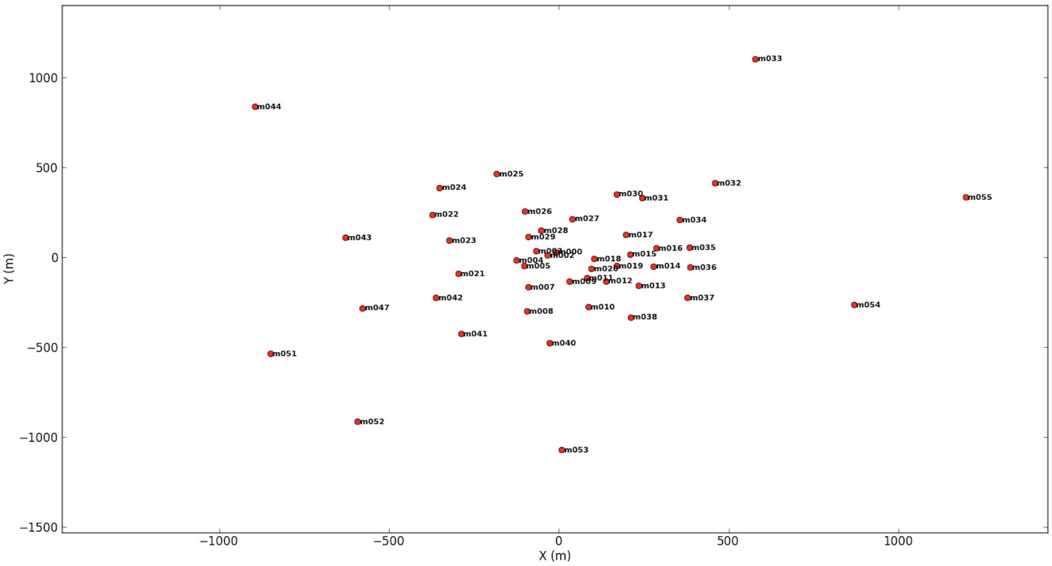

FIGURE 2.2: The MeerKAT core configuration. This shows the most dense region with a maximum radius from the core of approximately 1 km.

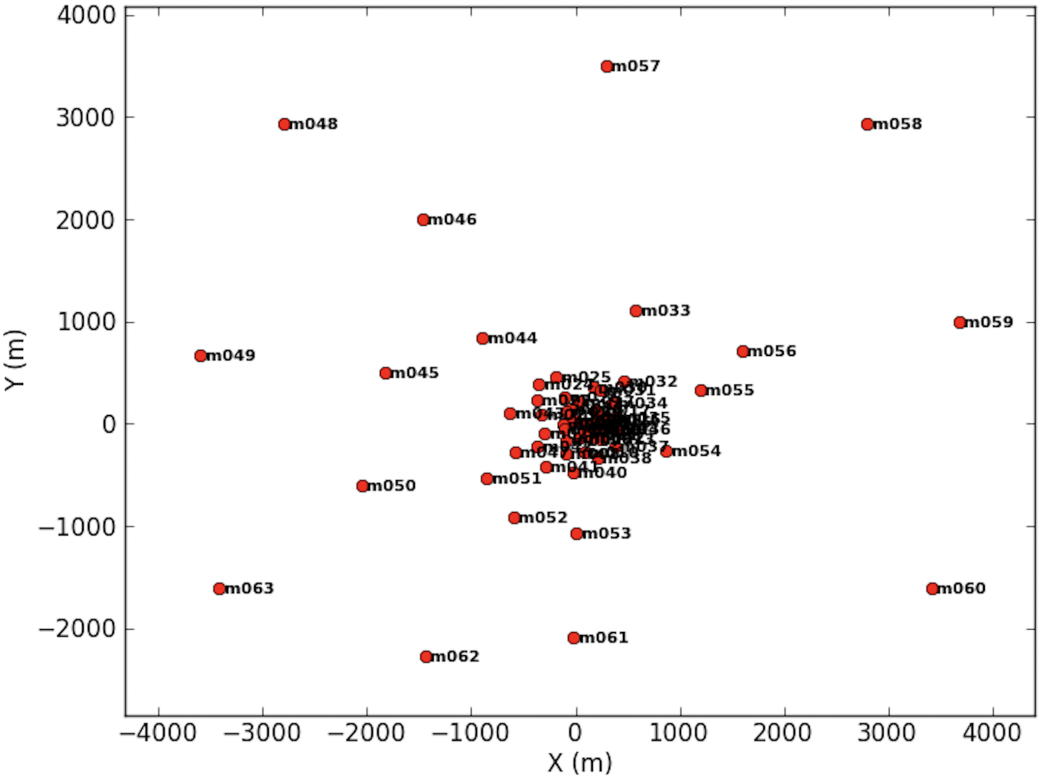

FIGURE 2.3: The full MeerKAT antenna layout. The majority of the antennas have short baselines and are central to the core.

2.2 Observations

Our observations of M87 were made on June 28th 2019. The integration time of the observations was 2 seconds, with 4096 frequency channels in the L-band (an 856 MHz wide band ranging from 856 MHz to 1712 MHz) centred at 1.28 GHz, in full polarisation mode. The target was observed in scans of 15 minutes, interspersed with 3 minute scans of the gain calibrator J1150-0023; the bandpass calibrator J0408-6545 (which also served as the flux calibrator) was observed once at the beginning and once during the target-gain calibrator observation in scans of 8 minutes; giving a total observation duration of 3.7 hours for the target, 40 minutes for the gain calibrator and 16 minutes for the bandpass/flux calibrator. The observational strategy followed the recommended practice for MeerKAT.

TABLE 2.1: MeerKAT observations.

Date	28 June 2019
Total frequency range	856-1712 MHz
Channel width	209 kHz
Integration time	2 seconds
Number of antennas	59
Bandpass/flux calibrator	J0408-6545
Gain calibrator	J1150-0023
Time on target	3.7 h
Time on J1150-0023	40 m
Time on J0408-6545	16 m
Pointing centre (J2000)	RA 12:30:49.40 Dec +12.23.28

M87 is a northern hemisphere source (Declination $\approx +12$ deg), thus giving the vertically flattened uv-coverage map in Figure 2.4. MeerKAT's dense core antenna configuration can be seen from its uv-coverage, there are more visibilities clustered around the centre and shorter baselines and fewer on the outskirts, just as MeerKAT has more short baseline antennas than it has long baseline antennas.

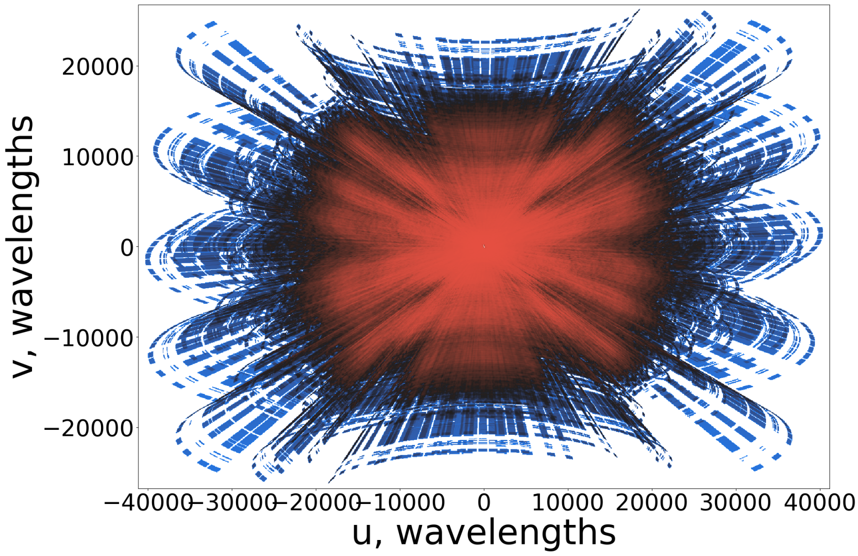

FIGURE 2.4: Full bandwidth uv-coverage of the MeerKAT observation of M87. The colour scheme denotes the density of the data points, with red points corresponding to the more densely sampled regions of the uv-plane and blue showing more the sparsely sampled regions.

In Fig. 2.5 we see the MeerKAT scale-dependent sensitivity of the M87 galactic structure. The radio core region, which is approximately 1.26 arcmin in extent, has a larger integrated flux than the large-scale, diffuse inner and outer halos, which span 6 arcmin and 14 arcmin, respectively. The baseline distribution illustrates which spatial models of M87 the MeerKAT L-band observations are preferentially sensitive to.

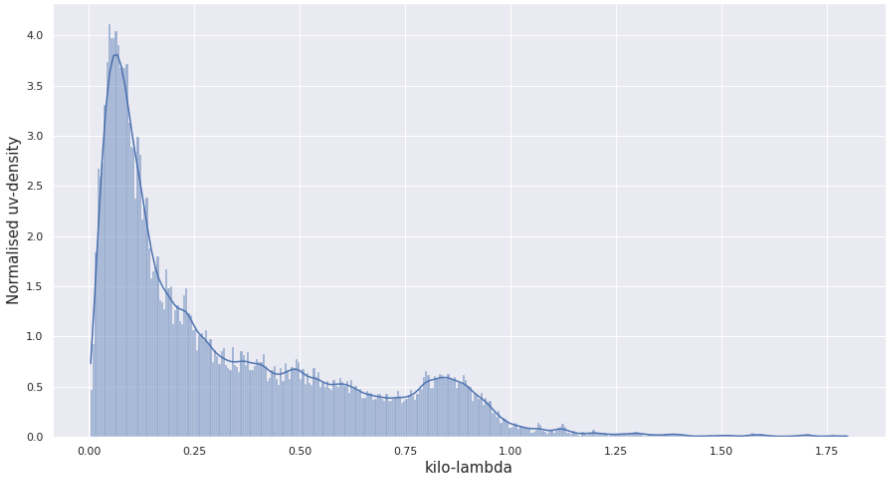

FIGURE 2.5: The normalised density of the number of visibility measurements in the data-set. This is a proxy for the MeerKAT sensitivity to the different components that make up M87, and their corresponding spatial models.

The L-band MeerKAT RFI occupancy comes from three main sources: **D**istance **M**easurement **E**quipment (DME) on aircraft, **G**lobal **S**ystem for **M**obile Communication (GSM) and **G**lobal **N**avigation **S**atellite **S**ystem (GNSS) satellites. The RFI environment is mapped over the M87 observation. The shorter baselines were observed to have stronger RFI detection than longer ones, this occurs because RFI tends to decorrelates with increasing baseline length.[2]. Fig. 2.6 and Fig. 2.7 show the relative strength of RFI as observed by a short and a long baseline.

2.3 Calibration

Cross calibration was performed using `oxkat`[3] (Heywood, 2020). We reduced our M87 data on the ilifu cluster. For self-calibration, M87 required a highly tailored approach, we used various methods which include making use of the pipeline software that we developed, `multi_image`[4], `stimela`[5] (Makhathini, 2018) scripts and miscellaneous non-scripted ad hoc methods. Our calibration pipeline, `multi_image`, is an ensemble of Python scripts that simultaneously perform multiple imaging-selfcal runs with various parameters. We make use of well-established software, such as `CASA` and `WSCLEAN` (Offringa & Smirnov, 2017).

2.3.1 Initial manual inspection

The `CASA` task `listobs` was used to obtain some information about the observation, i.e. the number of scans per field, the duration of each scan and so on. Some scans were erroneously shorter than expected, on the order of few tens of seconds, a known issue with the MeerKAT early science data. This caused the SNR for gain solutions (which are typically limited by scan boundaries) to drop, thus we flagged them out. These scans constituted 42% of all scans. The raw visibilities were inspected, as a sanity check, and nothing out of the ordinary was seen, for a typical MeerKAT data set.

Using `shadems`, we then plotted the gain calibrator's (J1150-0023) visibility-amplitude against uv-distance or baseline length in Fig. 2.8. The visibility amplitude is relatively constant for all baseline lengths, this means that the source is unresolved, i.e. essentially a point source. This is because the Fourier transform of a delta function (at the origin) is constant. In Fig. 2.9 we make a similar plot for the target, this time the amplitude drops sharply with increasing uv-distance. The interpretation of this phenomenon is that the source is well resolved.

---

[2] `https://skaafrica.atlassian.net/servicedesk/customer/portal/1/topic/bc9d6ad2-8321-4e13-a97a-d19d6d019a1c/article/305332225`

[3] Oxkat GitHub repository `https://github.com/IanHeywood/oxkat`

[4] For the repository refer to my GitHub page `https://github.com/LeonMtshweni/multi_image`

[5] `https://github.com/ratt-ru/Stimela`.

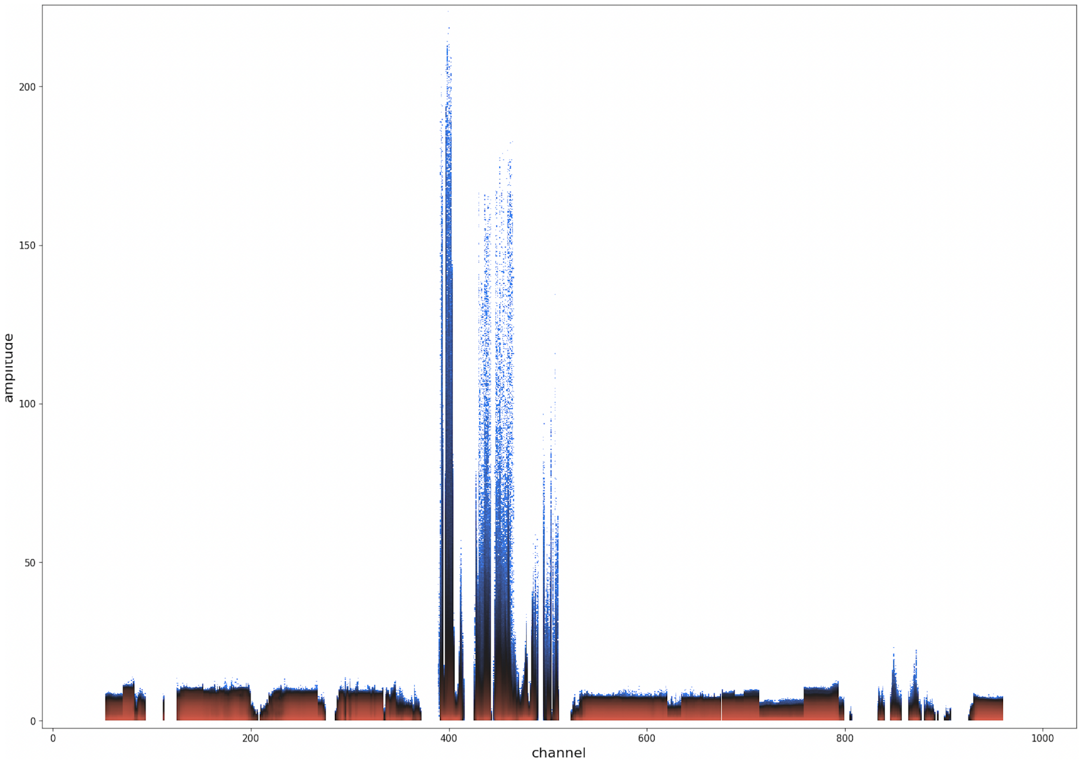

Figure 2.6: A plot of the amplitude as a function of channelised frequency for M87 over the baseline m000-m002. The RFI seen as high amplitude spikes, correlates, relatively, strongly for a short baseline.

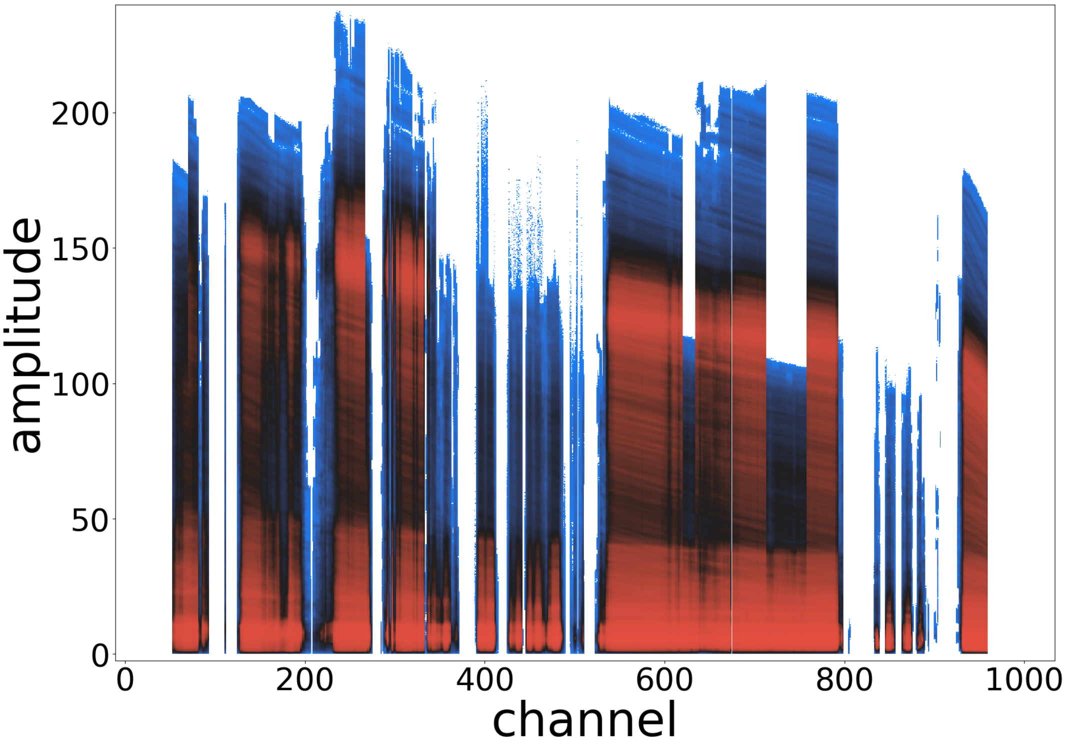

Figure 2.7: A long baseline counterpart of Fig.2.6. The RFI correlates more weakly on longer baselines.

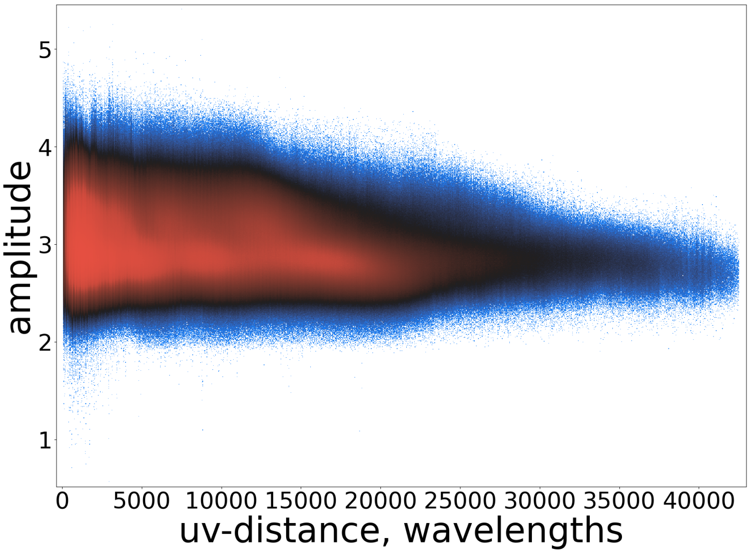

Figure 2.8: The amplitude as a function of uv-distance of a mostly unresolved source, the complex gain calibrator, J1150-0023.

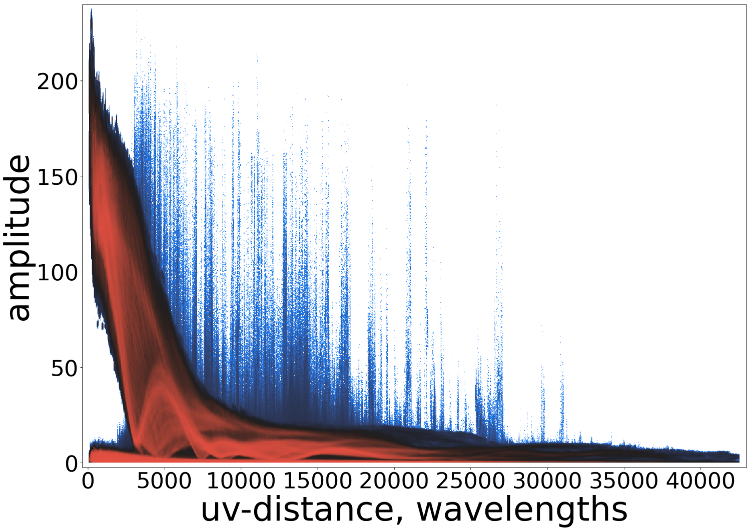

Figure 2.9: The amplitude as a function of uv-distance of M87. It can be seen that the source is resolved.

In Fig. 2.10 we show the observation strategy, the first source observed, J0408-6545 (the primary flux density and bandpass calibrator source), is the second brightest source and it is observed twice. The gain calibrator J1150-0023 is observed second interleaved with the target 3C274, the brightest source. Typically, the gain calibrator is brighter than the target, but not at all in this case, because M87 is quite a bright. Note that the spread in amplitudes is mainly caused by the fact that these are extended structures, thus the various baselines observe marginally different amplitudes. Even the point source structures have some finite size, there are no real point sources in reality.

A priori, we expected some challenges with the calibration and imaging for several reasons including:

1. The large integrated flux of $S_\nu > 300$ Jy.
2. The complex source structure limiting potential improvements expected from self-calibration.
3. The northerly location of the source resulting a sub-optimal MeerKAT PSF and resultant deconvolution challenges.
4. These data were acquired as part of early science observations and so were likely to contain some of the imperfections seen in other early data (e.g. erroneous scan lengths, spikes in the bandpass).

In the following sections, we detail our calibration and imaging strategy, along with our methodologies in mitigating these challenges and others.

2.3.2 Cross calibration

In this stage of the calibration `oxkat` follows a standard data reduction procedure, while making use of both common and bleeding edge software like `CASA` and `CubiCal`. The method begins by first averaging the 4k data in frequency to 1024 channels and in time to 8 seconds. Then the first flagging round, the bandwidth roll-off at the upper and lower edges of the band were removed. Then a host of L-band frequency ranges that coincide with known RFI sources such as GSM (900-915 MHz and 925-960 MHz) and GPS (L1, L2, L3, L5) were then flagged using the manual mode of `CASA` `flagdata`. This mode flags according to set instructions, a maximum uv-range limit of 600 m was used. Finally, the flagging mode was set to clip, which removes data according to set values. We set it to remove all zero-value data and to clip outside the range 0-300 Jy.

Absolute flux density

We used a manual flux-density scale of F_0 = 2.9 Jy, a spectral index of -0.042 and a reference frequency of ν =1.3 GHz for the spectrum of J0408-6545,

$$S_\nu = F_0 \cdot \left(\frac{\nu}{\nu_0}\right)^\alpha, \tag{2.1}$$

where S is the observed flux, $\alpha = \mathrm{s}_0 + \mathrm{s}_1 \log \frac{\nu}{\nu_0} + \ldots$, s_0 and s_1 are parameters which give information about the spectral behaviour of the source, ν_0 is the reference frequency. Further information can be found in NRAO's documentation for `setjy`[6].

---

[6] `https://casa.nrao.edu/docs/taskref/setjy-task.html`

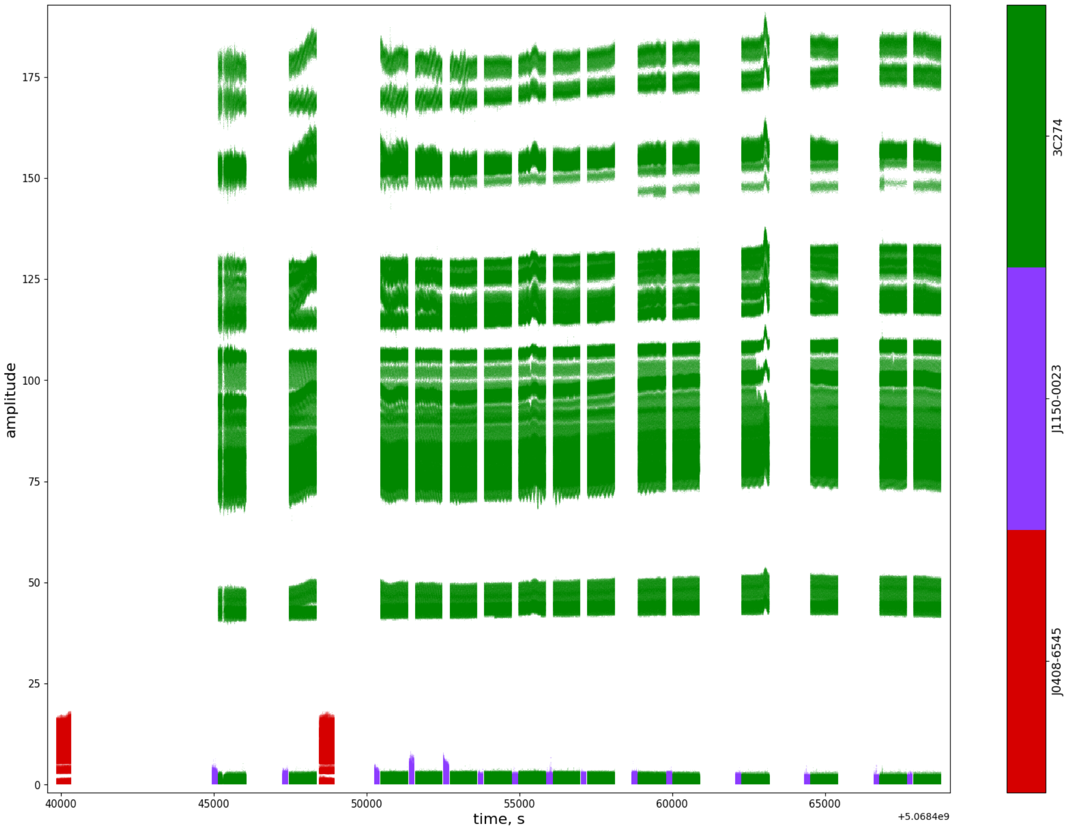

FIGURE 2.10: The amplitude versus time plot, i.e. basic outline of how the sources were observed, coloured by field. The gain calibrator is coloured purple (J1150-0023), the bandpass source red (J0408-6545) and the target green (3C274).

Flagging

After re-scaling the flux density, additional flagging was performed. The RFI was removed based on three flagging algorithms, namely, `rflag`, `tfcrop` and `extend`. `rflag` which removes outliers based on sliding-window rms filters, `tfcrop` that automatically identifies outliers on the frequency-time plane and `extend` which "extends" flags beyond what the basic algorithms detect.

`oxkat` splits the cross-calibration into 4 stages, that progressively improve the bandpass and gain solutions.

Stage 1: Initial Bandpass Calibration

Before we begin with the `bandpass` calibration using the standard calibrator J0408-6545, we performed an initial phase calibration, in order to average over the phase-time variations that may occur in the bandpass (and thus improving the SNR). We used the task `gaincal`, on the bandpass calibrator. Deriving the solutions in phase only, we use the `CASA` gain calibration type "**G**". The "**G**" type solutions generates a per-spectral window polarisation and time-dependent scaling factor. A bandpass solution was then created and applied to the visibilities. The associated solutions are shown in Fig 2.13 and Fig 2.14. To visualise our gain solutions we used `ragavi` [7].

These results were to be applied to the data, that is at each point in frequency the value of the visibility is going to be divided by the solution at the corresponding frequency. The ideal is for the corrected visibilities to have a constant value in amplitude as a function of frequency (i.e. channel) and to have zero phases for all frequencies, but of course this is not true in practice. We then apply these results, first applied to the secondary calibrator then to the target.

Stage 2: Improving the Bandpass solutions

Another round of phase-only `gaincal` was run on the primary calibrator, with the `bandpass` solutions from stage 1 being applied on the fly. Then an additional round of bandpass was run and applied with all previous calibration tables applied.

Stage 3: Initial Phase Calibration

A round of phase and amplitude gaincal was run on the primary calibrator J1150-0023 and the previous two solutions were applied as gaintables. Amplitude and phase calibration gain solutions were derived for the secondary calibrator. Then the actual flux density of the secondary is solved for, see Fig 2.11 and Fig 2.12. Similarly, these results were then applied to the primary calibrator, then to the target.

Stage 4: Improving the Phase calibration

Since the secondary calibrator has been flagged of any RFI that `tricolour`'s `tricolour` strategy could identify, we perform another, final, round of phase-only delay self-calibration on the secondary calibrator incorporating all previous gain solutions.

---

[7] `https://ragavi.readthedocs.io/en/latest/`.

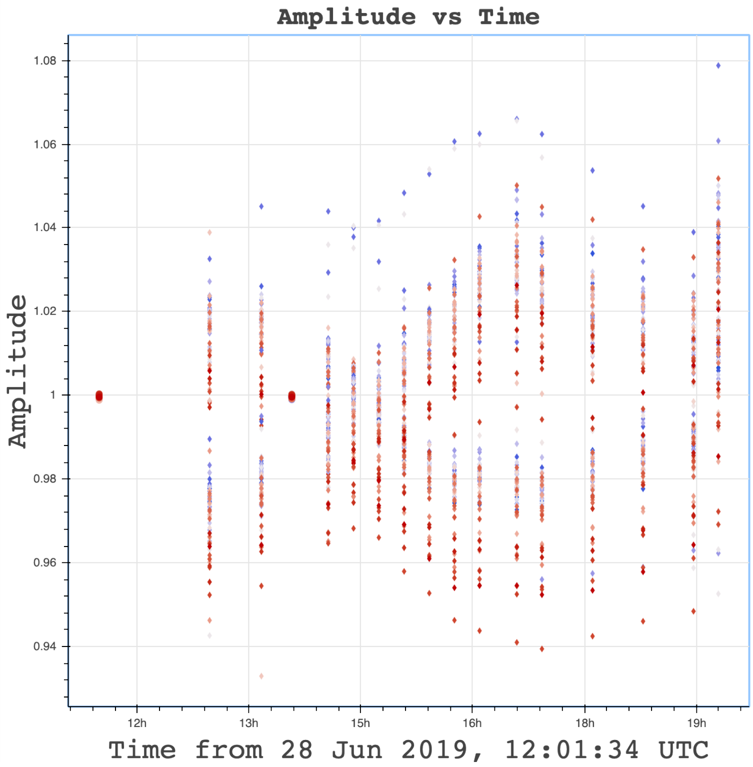

FIGURE 2.11: The amplitude versus time gain solutions, derived from the gain calibrator J1150-023. The `CASA` task `gaincal` was used in finding the solutions. A solution interval of 2 minutes was applied

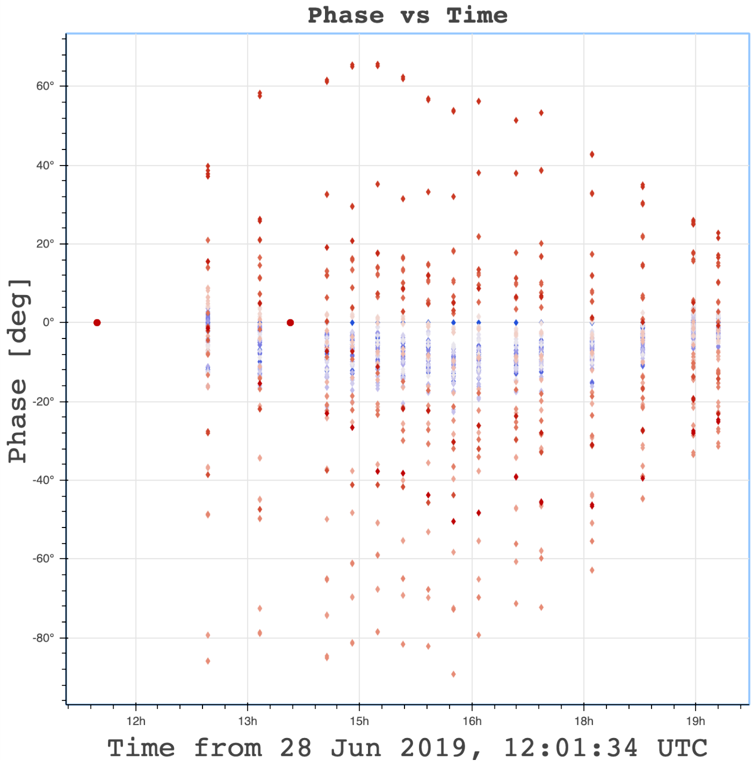

FIGURE 2.12: Phase corrections as a function of time, derived from J1150-023, using the `CASA` task `gaincal`.

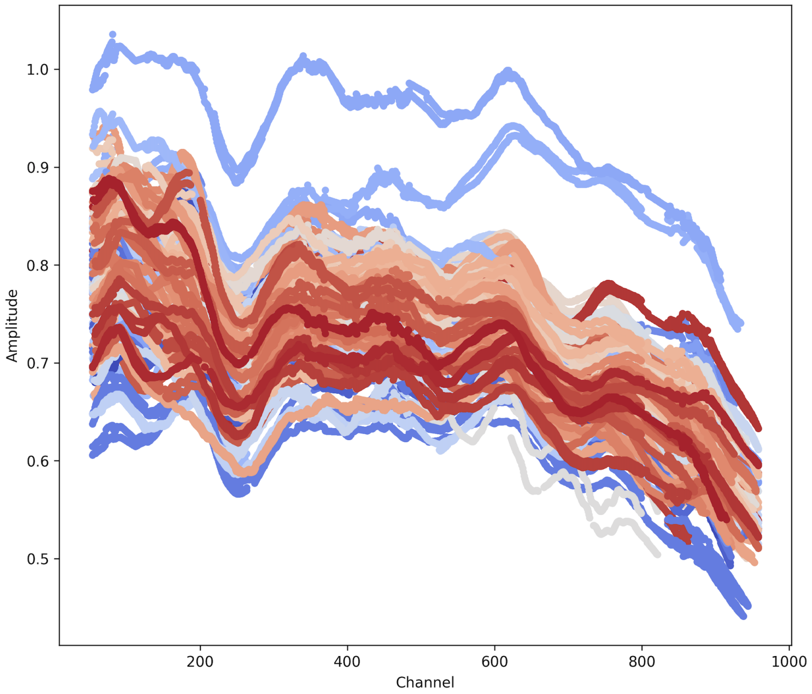

FIGURE 2.13: The amplitude versus frequency bandpass solutions. Derived from the flux/bandpass calibrator J0408-6545. The `CASA` task `bandpass` was used in finding the solutions. The data had channel width of 209 kHz and a frequency range of 856 - 1712 MHz

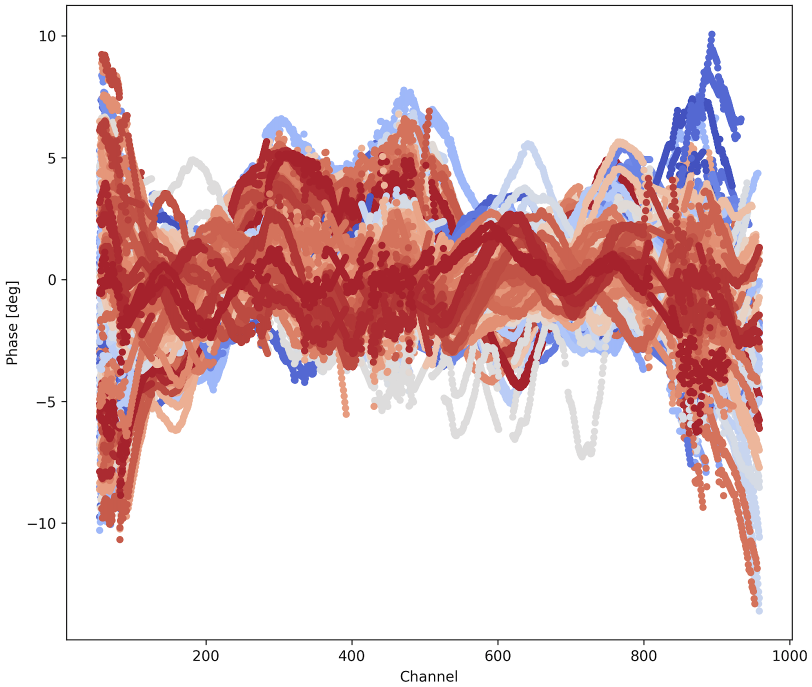

FIGURE 2.14: Bandpass phase solutions as a function of channelised frequency bandpass plots. The flux/bandpass calibrator J0408-6545 was used in deriving these corrections. The solutions were found using the `CASA` task `bandpass`.

2.3.3 Self-calibration

For self-calibration we wrote our own calibration pipeline software, which was necessitated by the fact that M87 is a bright complex source, thus we devised a highly tailored strategy to successfully image the source.

Calibration pipeline: `multi_image`

`multi_image`[8] is collection of `Python` scripts that perform multiple Multi-Frequency Synthesis imaging jobs with various imaging and self-calibration parameters. It is designed to work on a `slurm` based cloud infrastructure such as the ilifu cluster hosted by the **I**nter-University Institute for **D**ata **I**ntensive **A**stronomy (IDIA). Some of these imaging parameters include uv-range, masking, multiscale, weights, uv-tapering, etc. The point is to systematically explore the relevant parameter space more efficiently, and then too optimise the use of the key parameters.

Self-calibration with `CubiCal`

`STIMELA` uses `CubiCal` in deriving gain solutions. The way that `CubiCal` generates these solutions is that, the model is received from the imager, in our case `WSClean`, then `CubiCal` derives the gain corrections and applies them to the data. We shall discuss the rationale that went into making the choices for the various parameters that `CubiCal` offers.

Since RFI correlates more strongly over short baselines and taking MeerKAT's dense core layout into consideration (seen in Fig. 1.14), we chose not to calibrate baselines shorter than 150 m, using the parameter `sol-min-bl`. Calibrating for these baselines would run the risk of "cooking" RFI into our solutions, so it is best to not include these baselines when calibrating. We also clipped any gain solutions that went above an amplitude of 2.5 and below 0.5.

We used a weight spectrum to weight our data based on the level of noise. We solved for time-constant delays not accounted for by the correlator model, known as residual delays (Fig. 2.13 and 2.14). Small errors remain due to miscellaneous factors such as inaccurate antenna positions, environmental effects, timing. Delay calibration is not historically performed during self-calibration, but many in the community have found that it performs well in reducing some radial artefacts that may still be prominent in the data.

In selecting a solution interval (`CubiCal` parameter `time-int`), we had the task of selecting an interval that was small enough to pick up the gain variation, but not too small so that the gains were dominated by the noise. On review of the time intervals the data is split into, i.e. scans, we fit as many times of the `data-time-chunk` parameter into the data as would allow similarly sized data chunks. The aim is that when `CubiCal` derives the solutions the data is chunked in equally sized parts since in this way all the data chunks will be served by one solution interval.

---

[8] `https://github.com/LeonMtshweni/multi_image`

2.3.4 Imaging

In the first pass of the final imaging, no masks were used, we rather followed the method of lowering the `WSClean` parameter `threshold` consecutively as a stopping criterion. This parameter defines when to stop cleaning. The deconvolution will continue until the peak flux of the residual image is below this specified threshold. This is especially useful in cases where emission is not evenly detected, as was the case with M87's halo. This gave us the capability to deconvolve to a level just above the artefacts, which were at the Jy level.

An alternative parameter that sets how long you clean an image is the `niter` parameter. It allows users to set the maximum number of iterations to perform. We did not prefer this option as one cannot, easily anticipate the number of clean iterations needed to clean to the required depth for such a bright extended source.

In order to obtain a mask that captured the full extent of M87, while simultaneously excluding the artefacts and noise, we needed to devise ways to achieve our goal. After the initial cleaning, where the `threshold` option was used, `pybdsf`[9] was used to create an initial mask (Fig. 2.15). Despite our best efforts, `pybdsf` was unable to create an adequate mask, due to factors such as diffuse emission patches within the halo and strong artefacts that pervaded the image. To combat these issues we used a two-step process whereby we produced a mask using an M87 map, then using the image editing software `GIMP` (The GIMP Development Team, 2019) we improved upon it by manually editing the mask, using by-eye assessment to discern artefacts (Fig. 2.16).

Once the mask was made we then used the combination of `fits-mask`, `auto-threshold` and `auto-mask` to `CLEAN` deeper. This combination of parameters restricts the area in which `WSClean` performs the deconvolution. Occasionally we would switch back to using the `threshold` option to `CLEAN` outside of the mask area, then repeated the process. To reduce the PSF side-lobes we weighted the gridded visibilities using the `Briggs` weighting, with a `robustness` setting of -0.4. This choice is a trade-off between sensitivity and angular resolution.

Given that the theoretical MeerKAT maximum angular resolution at L-band is approximately 5.4 arcsec, we divided this value so that we can have 4 pixels across the beam, so as to sample the PSF adequately. We set enough pixels across to image up to the peak of the first pair of secondary side-lobes of the MeerKAT primary beam, which are at approximately 1.5 deg on either side, at 1.5 GHz. This resulted in an image of 9,000 × 9,000 pixels of size 1.3 arcsec × 1.3 arcsec.

In the final pass of final imaging, we enabled `multiscale` deconvolution with the following scales 0,10,20,40,80,160,320,400 and changed `Briggsrobust` to -2.0, since at this stage we would have improved our model image and could afford an additional loss to our image signal-to-noise-ratio.

---

[9] `pybdsf` is a versatile tool that, among other things, can export fits masks given an image. The documentation can be accessed here `https://www.astron.nl/citt/pybdsf/#`.

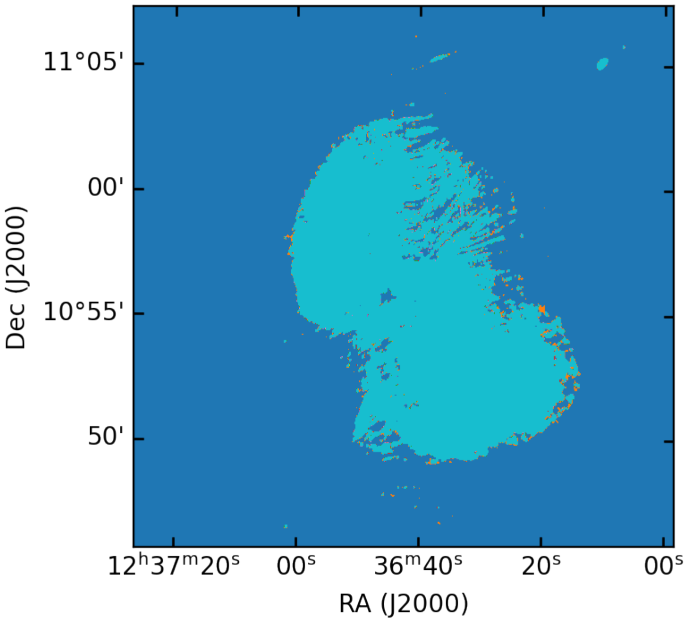

FIGURE 2.15: A `pybdsf` exported fits mask made using by using the M87 full intensity map.

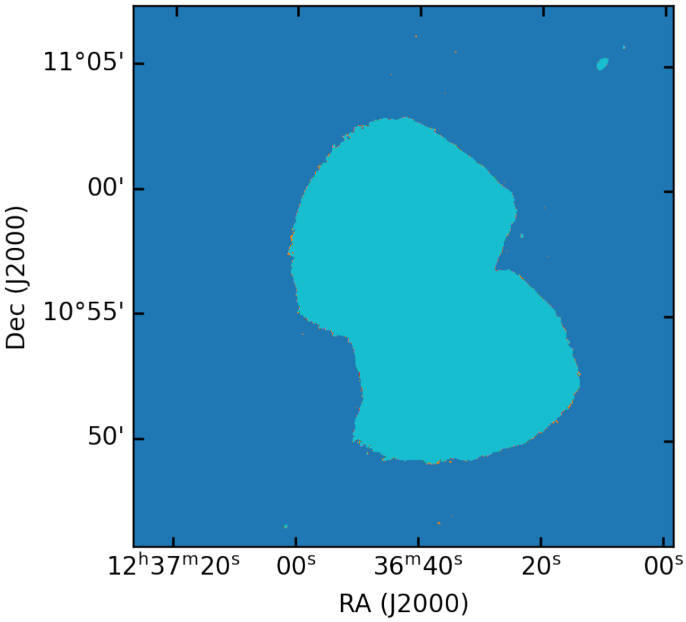

FIGURE 2.16: The same exported `pybdsf` fits mask with manual enhancements made with the image editing software `gimp`.

The entire band was used to make the main image of M87, in order to get the optimal uv-coverage and signal to noise ratio. We however broke down the large bandwidth into smaller sub-bands, called spectral windows. Each spectral window was deconvolved independently. `WSClean`'s parameter `channels-out` divides the data bandwidth by a specified number. It is common to use 8 spectral windows (perform deconvolution on 8 separate images in the band simultaneously), this is suitable in that it optimises the deconvolution time and the quality of deconvolved image. When this is complete, the various images were all put together with the parameter combination `join-channels` and `fit-spec-pol`. The `join-channels` parameter tells `WSClean` to join the sub-band images into a single **M**ulti-**F**requency **S**ynthesis (MFS) image. A polynomial is fit to the sub-images to "stitch" them together, we chose to use a linear fit, since we saw no apparent spectral dependency in M87's structure. This is performed by setting the `fit-spec-pol` parameter to 2.

Using `CubiCal` we derived delay and phase only solutions every 24 seconds of observation. The solutions were direction independent. The whole bandwidth was used when deriving solutions.

2.4 Software

We collate the various software used throughout our project.

Software	Description	Hyperlink
`PyBDSF`	Decomposes images into components	`ASTRON`
`CASA`	Calibration and Imaging software	`NRAO`
`stimela`	Data Pipeline	`RATT-GitHub`
`oxkat`	Data Pipeline	`IanHeywood-GitHub`
`shadeMS`	Plotting of visibilities	`RATT-GitHub`
`CubiCal`	Calibration software	`documentation`
`WSClean`	Imaging software	`documentation`
`AutoStacker`	Stacking and simulating visibility data	`ThatoEugine-GitHub`
`BRATS`	Tools for spectral analysis	`documentation`

Table 2.2: The main software packages used in our study and analysis of M87.

We will delve into slightly more detail when we discuss the use of each software, but as always the documentation is still the best place to read up about the various tools.

Chapter 3

Results

In this chapter we present a high dynamic range, L-band MeerKAT image of M87 and a discussion of its complex morphology. Then we detail a side-by-side comparison of our MeerKAT map with the Owen et al. (2000) VLA 327 MHz map and derive a MeerKAT-VLA spectral index map from the two maps. Followed by the MeerKAT in-band spectral index map. Finally, we calculate the minimum-energy requirements for the M87 halo.

3.1 Full resolution images

In Fig. 3.1 we show the full-bandwidth (770 MHz) M87 image as observed with MeerKAT at a central frequency of 1.28 GHz. The image in Fig. 3.1 was restored with a 2D Gaussian beam with a **f**ull **w**idth **h**alf-**m**aximum (FWHM) size of 10.4×6.9 arcsec and beam position angle 171.2 deg. The rms noise level is $\sigma = 0.5\,\mathrm{mJy/beam}$.

The enveloping emission (the halo) extends to a radius of 85 kpc and ends abruptly with limb-brightened extremes (Owen et al., 2000). The inner core (the cocoon) has a radius of approximately 5 kpc and contains both the core of M87 galaxy and the full extent of the optical and X-ray collimated jet. The halo and the cocoon are connected by an outflow. At the edge of the eastern outflow, there seems to have been a collision between the jet plasma and the ICM, which caused the outflow plasma to "roll-back" on itself to form the two lobes above and below the outflow, forming a vortex-like structure some times referred to as "The Ear". The western flow experiences a southerly bend and shows several filamentary structures. These observations are consistent with previous observations of the diffuse M87 radio structure (de Gasperin et al., 2012; Owen et al., 2000).

It seems the dense atmosphere of the cluster that M87 sits in has had an impact on the anomalous morphology of M87. This is seen in other radio sources that sit in the centers of galaxy clusters (Bohringer et al., 1995b; Burns, 1990; Fabricant et al., 1980). The halo has a sharp surface brightness drop-off relative to the core. The edge-brightening the halo exhibits implies that the halo ends abruptly and that it may be expanding. The MeerKAT halo contains a number of complex features, that are quite similar to the filamentary structures previously shown in Owen et al. (2000).

A central core region houses the supermassive black hole and is the engine that powers to well collimated jets. The two poorly collimated outflows that emerge from the core are referred to in this work as the inner-lobes. Fig. 3.3 shows two "bubbles" encapsulating two inner-lobes and the central bright core. These bubbles, we shall refer to as the northern and southern hemispheres of the halo, seem to overlap around the central region of the galaxy and continue undisturbed from the inner lobes to the outer edge of the radio halo and abruptly end with well-defined outer boundaries.

Morphologically, the MeerKAT image bears a strikingly similar appearance to the VLA 327 MHz map, despite the vastly different observing frequencies, image reconstruction algorithms, and radio interferometers used. Fig. 3.1 is consistent with the results from Owen et al. (2000) and de Gasperin et al. (2012). However, there are some deviations, for example, there is emission "missing" from the MeerKAT map in the region just left to Feature A. This observation is consistent with the spectral index analysis of M87 by de Gasperin et al. (2012), who measured a steep spectral index between 100 MHz and 327 MHz. We shall discuss the spectral index study further in Section 3.3, but first we make a detailed comparison between the MeerKAT and VLA maps.

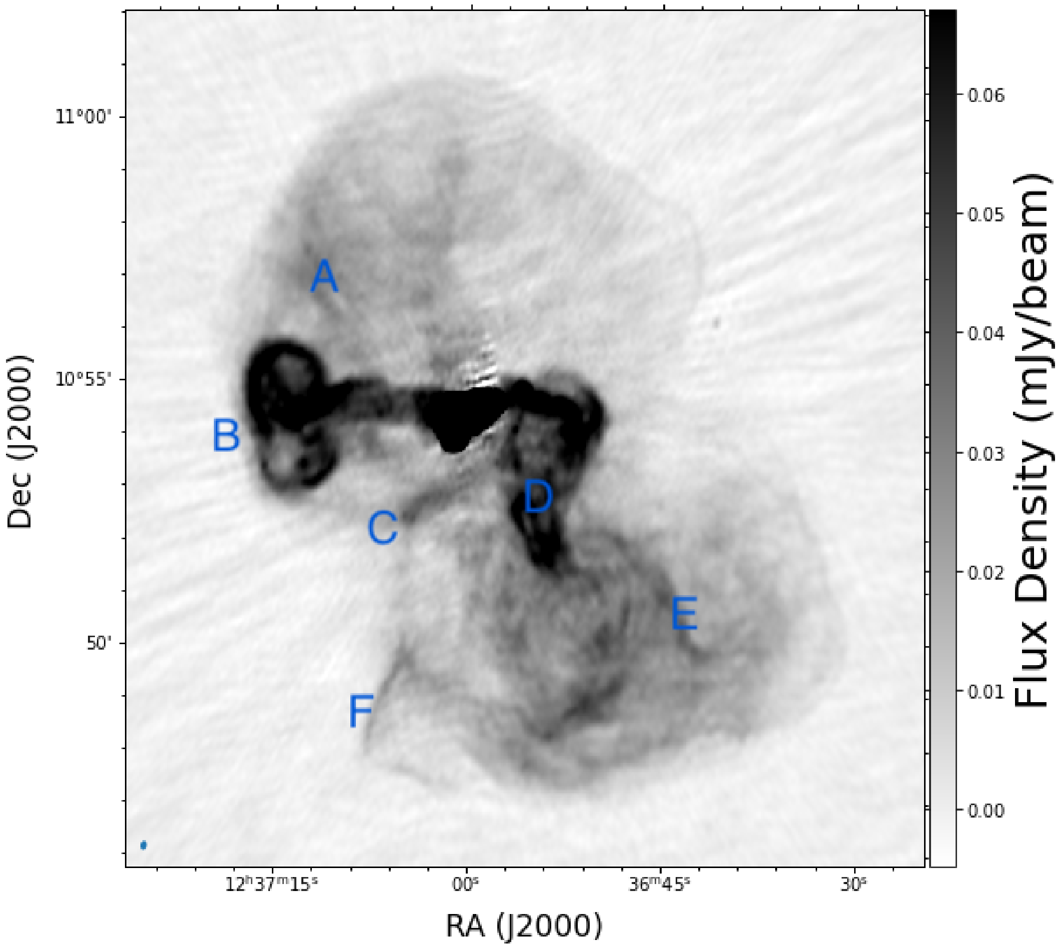

Figure 3.1: The MeerKAT total intensity image of M87. The total `CLEAN`ed flux density at 1.28 GHz is approximately 248 ± 1.20 Jy. The map is dynamic range limited, with a measured rms the rms noise level $\sigma = 0.5$ mJy/beam and the restoring beam size is 10.41 arcsec × 6.90 arcsec, beam position angle 171.21 deg.

3.2 A comparison of the MeerKAT and VLA M87 maps

In this section we give a more in-depth comparison between the MeerKAT 1.28 GHz and the VLA 327 MHz M87 maps. The VLA and MeerKAT maps of M87 are the two most detailed maps of the M87 complex halo and are, quite subjectively, the best maps in existence of the complex halo structures of M87 because they are the only maps that resolve the complex filamentary halo structure, amongst other reasons. Fig. 3.3 and Fig. 3.4 show the full scale, total intensity maps of M87 as captured by MeerKAT and VLA.

Given such a significant frequency difference between the MeerKAT and VLA maps, in order to have a somewhat meaningful feature comparison, we made a flux density reference map. It is derived from the VLA map but with a flux density that would be consistent with an assumed uniform $\alpha = -0.7$ spectral index value.

There is a positional offset between the two maps, partly because the self-calibration process loses absolute astrometic precision of the images, but mainly because the VLA image is registered in the B1950 epoch and the MeerKAT image in the J2000 epoch. Removal of these positional differences is important for the computation of the spectral index map, since any inaccuracies in position would result in different regions of the galaxy being compared in the spectral index map.

Our method was to use the core to co-register the images on the same astrometric frame. While this does not address absolute astrometry, our interest here is only on the accurate relative astrometry to perform the spectral index analysis. We use two methods with differing levels of accuracy,

1. The small angle approximation calculation, where no on-sky projection effects are taken into consideration.
2. The great-circle distance (spherical distance) computation, which takes projection effects into account.

Method (2) proved to be more accurate than the first, since method (1) would still result in sub-arcsecond mis-alignments between the images. We received the VLA map with all of the off-central axis sources removed, with approximately 500 × 600 pixels. To generate the spectral index image in Fig. 3.5, we first had to re-grid the image so that the image data arrays had the same dimensions and that the pixels were the same size. Then, by eye, identified the positions of the brightest pixels in both images. Then we converted the image pixel position of the brightest feature to its corresponding on-sky angular coordinates. Using `astropy` we calculated the separation in degrees and subtracted the offset from the VLA image, to re-position it. The spectral index image was then derived by fitting a linear model to each pixel between the two images.

In this section, we present the two point spectral index image, derived from the central frequencies of the images, 327 MHz and 1.28 GHz. In order to make a spectral index from different telescopes we need to ensure that similar spatial modes are compared, that is, that the $uv-$coverage of the two telescopes are similar or, at least, have an overlap.

In order to ascertain that the MeerKAT and VLA $uv-$coverage were similar we required to compare the two and given that we only had the image data for the VLA and not the actual visibilities, we simulated a VLA data-set. Making use of the project code of the VLA observation (found in the fits header), we looked up the bandwidth, number of spectral channels, integration time and the total observation time of the observation in the NRAO VLA archive. Using this information and a modified excerpt of `AutoStacker`[1,2], we simulated a hypothetical VLA measurement set with the above mentioned parameters. This simulated data-set attempts to "mimic" the Owen et al. (2000) observation. We make the assumption that the observation duration is centered on hour angle $= 0$.

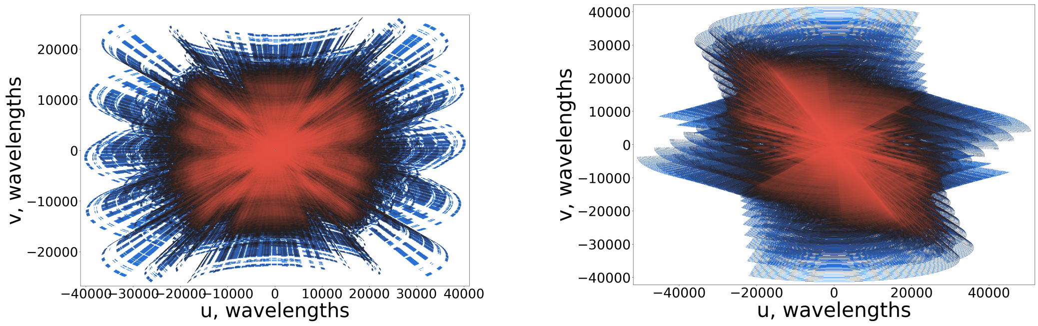

(A) MeerKAT (B) VLA

FIGURE 3.2: The uv-coverage of the MeerKAT and VLA M87 observations, in wavelengths. The VLA and MeerKAT sample similar spatial scales. The colour axis represents the density of data points, with red regions having higher density than blue regions. The VLA data was simulated to be in the A and B configurations.

The combined A and B configuration on source time for the VLA data was 17.8 hrs as compared to the sub-four hour (3.7 hrs) MeerKAT observation. The time integration were 10 and 2 seconds for VLA and MeerKAT, respectively. 1024 spectral channels for the MeerKAT observation and 32 for VLA. A 3.1 MHz bandwidth in the VLA observation and a 856 MHz for the MeerKAT observation. Table 3.1 summarises this information. In Fig. 3.2 both MeerKAT and VLA have uv-coverage up to 20 kλ, that is 4.6 km in units of projected baseline lengths. There is an overlap in the $uv-$coverage up to, at least, 3000 wavelengths, thus justifying a comparison of the two maps.

---

[1] A python module that simulates and performs stacking in the image and visibility domains of MeerKAT data.

[2] For the full software please visit the repository `https://github.com/thatoeugine/AutoStacker`

	MeerKAT	VLA
Bandwidth	856 MHz	3.1 MHz
Time on Source	3.7 hrs	17.8 hrs
Channels	1024	32
Integration time	2 seconds	10 seconds
Central frequency	1.28 GHz	327 MHz
Fractional bandwidth	856 MHz	3.1 MHz
Number of antennas	59	27

Table 3.1: Observation details for the VLA and MeerKAT images.

The imaging software used for the VLA map was the **max**imum **Ent**ropy (maxEnt) based `VTESS`[3]. The strongest appeal of using `VTESS` is that the maps come out with large-scale emission that seems to be more visually pleasing than those obtained using the CLEAN algorithm or its derivatives, given that CLEAN's fundamental assumption is that the sky brightness distribution can be decomposed into a set of point sources[4]. In addition, the `VTESS` maps only contain positive emission.

The VLA map has no restoring beam, a property of the imaging software, so the units are in flux/pixel. As is typically performed with MaxEnt methods (Event Horizon Telescope Collaboration et al., 2019b), the model image is convolved with an elliptical Gaussian beam having a full width half-maximum (FWHM) diameter of 10.4 arcsec × 6.9 arcsec and a position angle of 171.2 deg, to match the MeerKAT image. A final note is that in constructing the VLA map, the residual is not added to the restored map. The integrated radio flux density at 327 MHz, as detected by the VLA, is 108 Jy and the rms noise is 45 μJy/pixel, as estimated by the `CASA` tool `imfit`.

In Fig. 3.3 and Fig. 3.4 we plot the MeerKAT and VLA maps, set to the same colour scale. In both images we see a northward spur. The spur emanating from the core seemingly merges into diffuse emission of the halo. Furthermore, Feature A is present in both maps, just not seen as prominently in the MeerKAT map. This feature continues to form a loop northwards of The Ear quite prominently.

This is quite interesting as the spectral index map (shown in Fig. 3.7) shows no evidence of these linear structures, there is, however, a general steepening in the region. This faint region also coincides with the deficit in the X-ray emission profile (Fig. 1.12), referred to as X-Ray cavity by Forman et al. (2007). A noteworthy comment is that de Gasperin et al. (2012) observes steep spectral indices in this faint emission $\alpha^{10\mathrm{GHz}}_{30\mathrm{MHz}}$=-1.23 ±0.02. The features could possibly be under the VLA and MeerKAT's detection limit.

Unlike the VLA image, the MeerKAT image contains negative clean components and

---

[3] This is an AIPS task which implements a forward-modelling Maximum **E**ntropy **M**ethod (MEM).

[4] This is described in this NRAO documentation `http://aips.nrao.edu/cgi-bin/ZXHLP2.PL?VTESS`

has the residuals added back to the restored map. Therefore, the map shows some aspects of the very issues that motivated `VTESS` to be used rather than `CLEAN` for the VLA observation, i.e. strong artefacts due to the residual being added back and poor quality models.

In both images the top halo is not as filamented as the lower half. The halo seems to be well defined across its entire periphery. From our point of view the halos overlap. There is a general decrease in surface brightness spanning almost half of the region. This decrease is due to energy losses associated with the work performed to fill the expanding volume of the halo in combination with synchrotron cooling.

In Table 3.2, we see that most of the structures are visible to a similar extent in the two images, with the exception of features A and C. This could be threaded emission, as seen in some new MeerKAT images (Condon et al., 2021; Ramatsoku, M. et al., 2020). Unsurprising to see due to the brightness sensitivity, dynamic range, and angular resolution of MeerKAT. Feature A is seen with more sharp detail in the VLA image.

Structural feature	MeerKAT	VLA
A	Discernible	Prominent
B	Prominent	Prominent
C	More Resolved	Discernible
D	Prominent	Prominent
E	Prominent	Prominent
F	Prominent	Prominent

TABLE 3.2: Refer to Fig. 3.1 for the labelled structures. The majority of the features are similar in appearance with the exception of two.

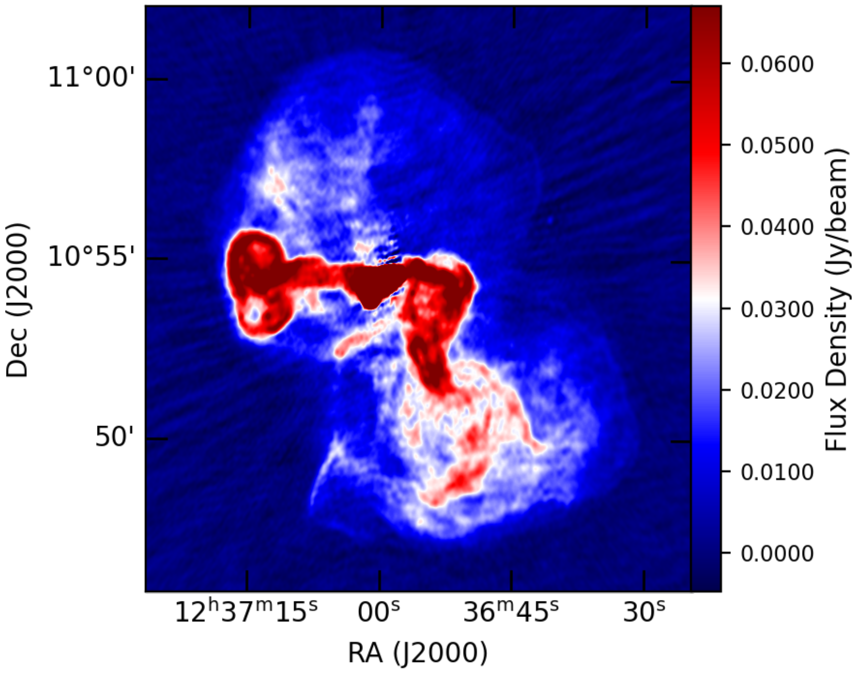

FIGURE 3.3: The MeerKAT 1.28 GHz M87 image. We chose a divergent colour-map because using it with a linear scale highlights the complex features of the halo and the limb-brightened edges. Which are both key for understanding the different structures of the radio source.

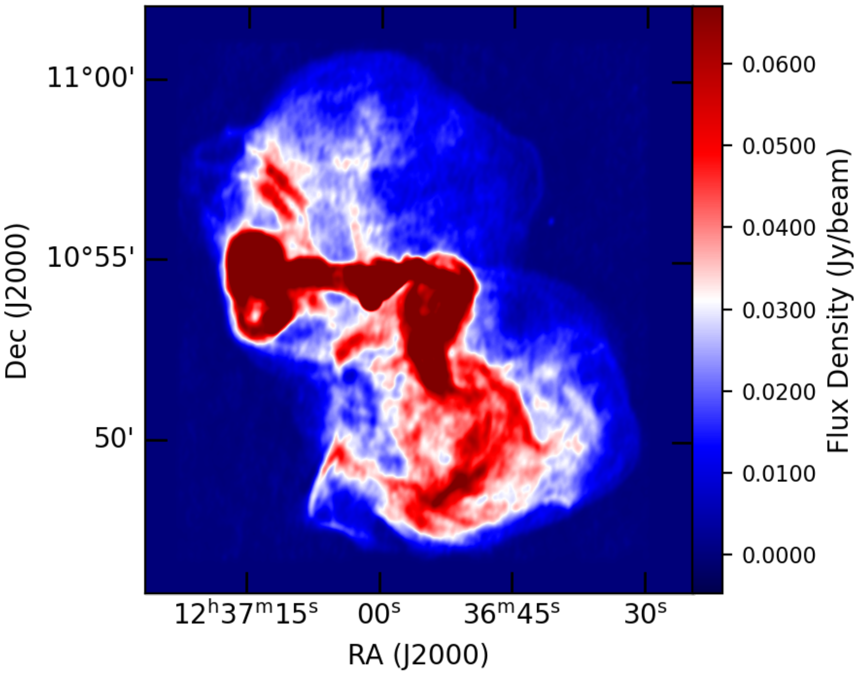

FIGURE 3.4: The VLA 327 MHz M87 image, re-gridded to match the image parameters of the MeerKAT image. It is also set to the same reference frequency as the MeerKAT map assuming all emission has a spectral index of α=-0.7, as explained in the text. Data from Owen et al. (2000).

We have two major differences - superior imaging quality with MeerKAT for large-scale sources, as well as a much larger data volume which precludes practical exploration of maxEnt methods. `CLEAN` images can be used for quantitative studies, the disadvantage of using the `CLEAN` algorithm is that the models are mottled[5], this can be seen in Fig. A.4 in the Appendix. We summarise these details in Table 3.3.

	MeerKAT	VLA
Centre Frequency	1.28 GHz	327 MHz
Imaging Algorithm	`WSClean`	`AIPS/VTESS`
Method	$\texttt{w}-\texttt{stackingCLEAN}$	`maxEnt`
Number of pixels	9000×9000	538×574
Pixel scale	1.3 arcsec	1.3 arcsec
Off-axis sources	Included	Pre-subtracted

TABLE 3.3: Image details for the VLA and MeerKAT images. Take note that the pixel-scale in the VLA map refers to the re-gridded image.

In Fig. 3.5 we show a close-up of the core and inner-lobe regions, revealing the M87's intricate features and lobes more clearly. Feature B ("The Ear") is observed at the same level of detail in both maps. Refer to Fig. 3.1 for a labelled diagram of M87. The upper half of the structure is more brightly illuminated than the lower half of the structure. In both images, the structure connects with the poorly collimated outflow that emanates from the core.

We computed the spectral index map based on the integrated fluxes from the images. To measure the flux densities, we outlined a region in the image encompassing the halo and fit elliptical Gaussian components to it, using `imfit` from `CASA`. This gave estimates in the flux densities, accurate to ± 1.6 Jy. The measured average spectral index is α_{327}^{1280} = -0.99 ±0.3. This value is in-line with the de Gasperin et al. (2012) spectral index of α_{100}^{327} = -1.19±0.02.

---

[5] Appearing to be covered in spots.

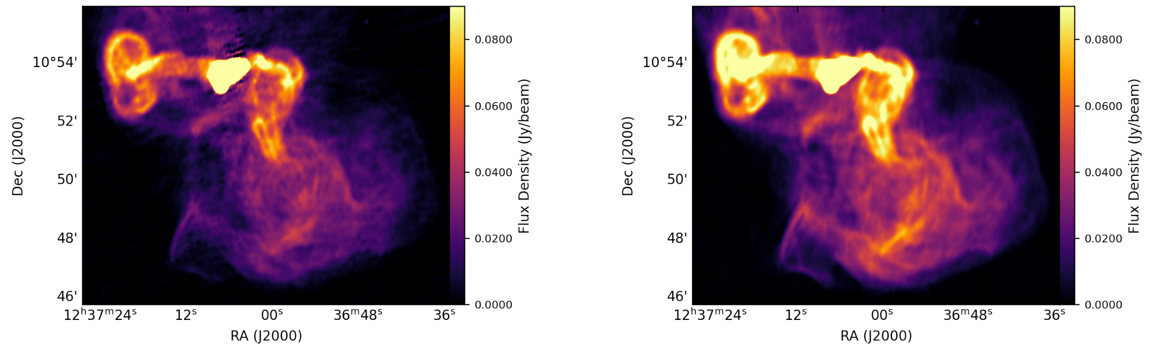

(A) MeerKAT

(B) VLA

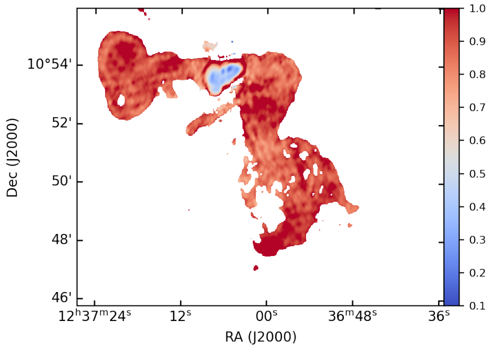

(C) Two point VLA-MeerKAT spectral index image

FIGURE 3.5: Left shows the MeerKAT 1.28 GHz image of the M87 core and inner-lobes. Right shows the same region of M87 at 327 MHz, imaged with the VLA. Bottom: the spectral index map between the VLA 327 MHz and MeerKAT 1.3 GHz points. Feature C, to the south of the inner core, is quite prominent in the spectral index map.

Both total intensity maps have a cavity towards the edge of the lower half of the structure. This could perhaps be a region of low magnetic field and/or low particle number density. The outflow that connects with Feature B has southerly emission, which seems to be distinct to the poorly collimated outflow, which in turn, may be connect to feature C. This is more readily seen in the MeerKAT image, but there seems to be hints of it in the VLA image and the LOFAR spectral index map (see Fig. 1.16(d)). The spectral index of this region is relatively steep, ranging between $-0.8 \leq \alpha \leq -1.0$. The cavity we noted earlier is also seen in the spectral index map.

The southward halo is highly filamented to similar extents in both maps. Feature C is seen at greater detail in the MeerKAT map than in the VLA map. Its spectral index is in the ranges between $-0.6 \leq \alpha \leq -1.0$, which is consistent with the values of the halo (Owen et al., 2000; de Gasperin et al., 2012).

The core of M87 galaxy has a spectral index of α_{327}^{1280} = -0.51, as is common for the cores of radio galaxies. Generally speaking, the spectral index is typical for active galaxies like M87. There is, however, a steepening of the spectral index as we move farther from the core, as can be seen in Fig. 3.7. The creation of Fig. 3.7 required that we convolve the sub-band images to a common beam

Zooming in on The Ear in Fig. 3.6, parts of the emission from the VLA image are over-saturated when both are set to the same contrast levels. The mean spectral index of the region is α_{327}^{1280} = -0.90 ±0.3. The Ear seems to have a torus geometry and resembles the later stages of slowly rising buoyant bubbles formed by powerful explosions. These bubbles may possibly have been inflated earlier during the nuclear active phase of the galaxy (Churazov et al., 2001).

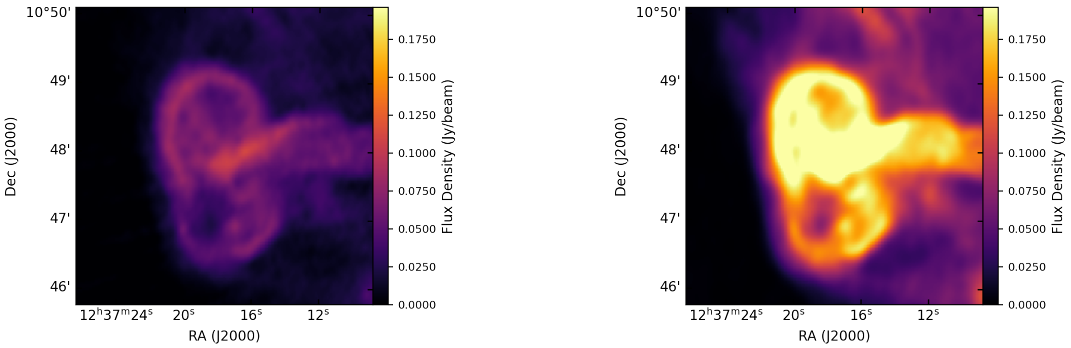

(A) MeerKAT

(B) VLA

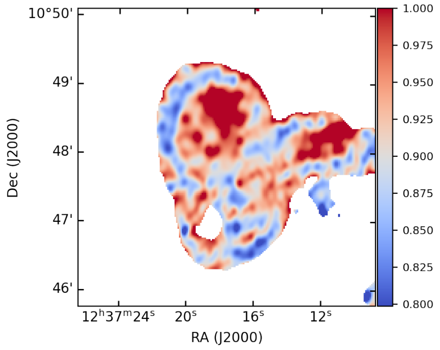

(C) Two point VLA-MeerKAT spectral index image

FIGURE 3.6: A zoomed in plot of the ear-like structure with the corresponding spectral index image. This image shows that the brighter parts of the vortex are younger, with a slightly flatter spectral index.

The feature would first start with spherical geometry, i.e. a bubble. Its transformation from a bubble into a torus is a common and well-known property of buoyant bubbles with weak surface tension (Walters & Davidson, 1963). During this transformation, some surrounding gas is captured and rises with the torus (Churazov et al., 2001).

It is through these slowly rising buoyant bubbles, that there is an explanation of the strongly correlated radio and X–ray morphology of the central 40 kpc region of M87 (Churazov et al., 2001). As the bubbles rise, they transport massive amounts of heat to the outward. Denser regions in the thermal gas, that rise with the bubbles, may fall back towards the central region and thus producing filamentary structures, which are consistent in radio and X-ray frequencies. These filaments would then trace back radially from the central region (Churazov et al., 2001).

3.3 Narrow band images and in-band spectral index map

We created an in-band spectral index map, made possible by MeerKAT's large fractional bandwidth. The 856 MHz wide band was split up into 8 sub-bands with central frequencies $\mathbf{SB}_0$ (0.9 GHz), $\mathbf{SB}_1$ (1.0 GHz), $\mathbf{SB}_2$ (1.12 GHz), $\mathbf{SB}_3$ (1.23 GHz), $\mathbf{SB}_4$ (1.34 GHz), $\mathbf{SB}_5$ (1.44 GHz), $\mathbf{SB}_6$ (1.55 GHz) and $\mathbf{SB}_7$ (1.66 GHz). Each sub-band has a 107 MHz bandwidth. However, $\mathbf{SB}_3$ and $\mathbf{SB}_7$ were excluded due to their high RFI occupancy. Refer to Table 3.4 for the noise rms and dynamic range of each image. In the table, the noise and dynamic range remain relatively consistent over all the sub-images.

In making the spectral distribution map, we convolved all sub-images to the lowest resolution image, $\mathbf{SB}_0$, i.e. the largest beam with dimensions 11.9 arcsec × 7.9 arcsec. The spectral index map was created using the Broadband Radio Astronomy ToolS (`BRATS`)[6] (Harwood et al., 2013, 2015) with a source detection limit of 12σ. We set such a large threshold due to data issues, lower σ cut-offs gave a grossly unreliable spectral index. `BRATS` is an application which provides a variety of tools for spectral analysis of broad and narrow bandwidth radio images.

Sub-image	Freq ν_0 [10^9]	RMS Noise mJy/beam	Dynamic Range [10^3]
$\mathbf{SB}_0$	0.91	3.28	7.1
$\mathbf{SB}_1$	1.02	1.54	13.9
$\mathbf{SB}_2$	1.12	1.75	10.1
$\mathbf{SB}_3$	1.23	1.75	5.9
$\mathbf{SB}_4$	1.34	0.89	15.1
$\mathbf{SB}_5$	1.44	0.83	13.8
$\mathbf{SB}_6$	1.55	1.35	8.4
$\mathbf{SB}_7$	1.66	1.75	7.5

Table 3.4: A summary of the image parameters of the various sub-band images. Note that we leave out $\mathbf{SB}_3$ and $\mathbf{SB}_7$ in the creation of the spectral index map. The dynamic range is defined as the ratio of the rms noise to

A comparison between the MeerKAT in-band spectral index map with the de Gasperin et al. (2012) (the LOFAR map) and the MeerKAT-VLA (the two point map) spectral index maps follows naturally. We shall first discuss the similarities between all the maps, then their inherent differences. In all three maps, we see a consistent spectral index for the core region, which falls within the range $-0.5 \leq \alpha \leq -0.55$, across all maps. This falls in-line with the expected values for compact core active galaxies. A general steepening of the spectral index is seen as we move farther from the core and into the halo of M87.

---

[6] `http://www.askanastronomer.co.uk/brats/`.

We measure a steep MeerKAT in-band average spectral index, α_{909}^{1551} = -1.4, in the in-band map, which strays quite far from the average values measured in the LOFAR, α_{100}^{327} = -1.19, and the two point, α_{327}^{1280} = -0.99, average spectral index values. This suggests significant spectral steepening between the LOFAR frequencies and MeerKAT frequencies, which is consistent with published radio spectral energy distribution in this range of frequencies. However, caution must be applied when interpreting the MeerKAT in-band spectral index map. Being at lower frequencies, the LOFAR map probes an older electron population, thus a spectral index of -1.19 is consistent with expectations. It is especially in this low-frequency map that we see evidence of the X-ray cavity, northeast of the map, seen as the green-black region in Fig. 3.8.

Alternatively, given that there is such a difference between the low- and high-frequency spectral index values, there may be a spectral break that exists between the frequency bands of the maps. In Fig. 3.9[7] we show a MeerKAT narrow band spectral index, derived from the frequencies in the range 1026-1250 MHz. Here we were able to set the threshold to a lower value of 5σ. The average spectral index of Fig. 3.9 is α_{1026}^{1250} = -0.99. Which is quite similar to the two point and the LOFAR spectral index values, thus reinforcing the possibility of a spectral break existing between the frequencies 1256 MHz and 1661 MHz.

---

[7] The lo-band data was independently calibrated.

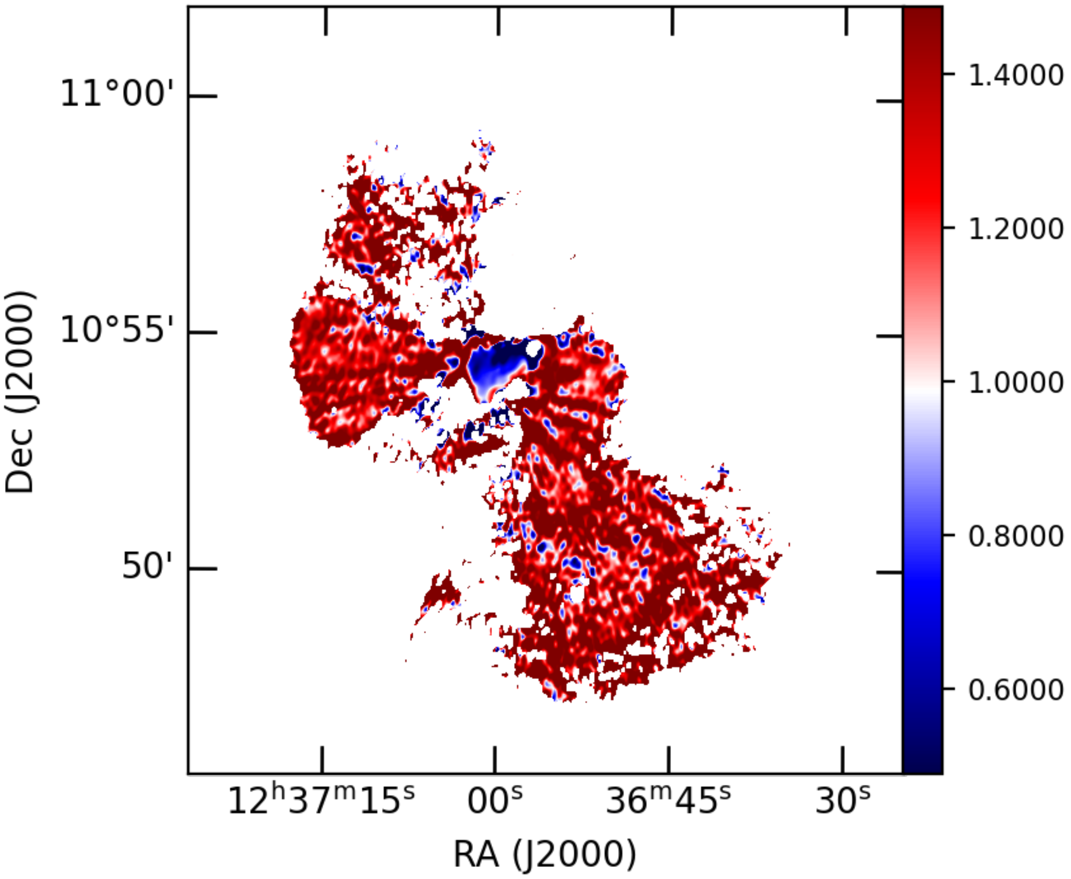

FIGURE 3.7: An in-band MeerKAT spectral index map of M87 obtained from the frequency ranges 856-963, 963-1070, 1070-1177, 1284-1391, 1391-1498 and 1605-1712 MHz. The various sub-band maps were smoothed to a common beam of 12 arcsec × 8 arcsec, using the `CASA` task `imsmooth`. Pixel values below 12σ in the respective images were excluded to obtain reliable spectral index values.

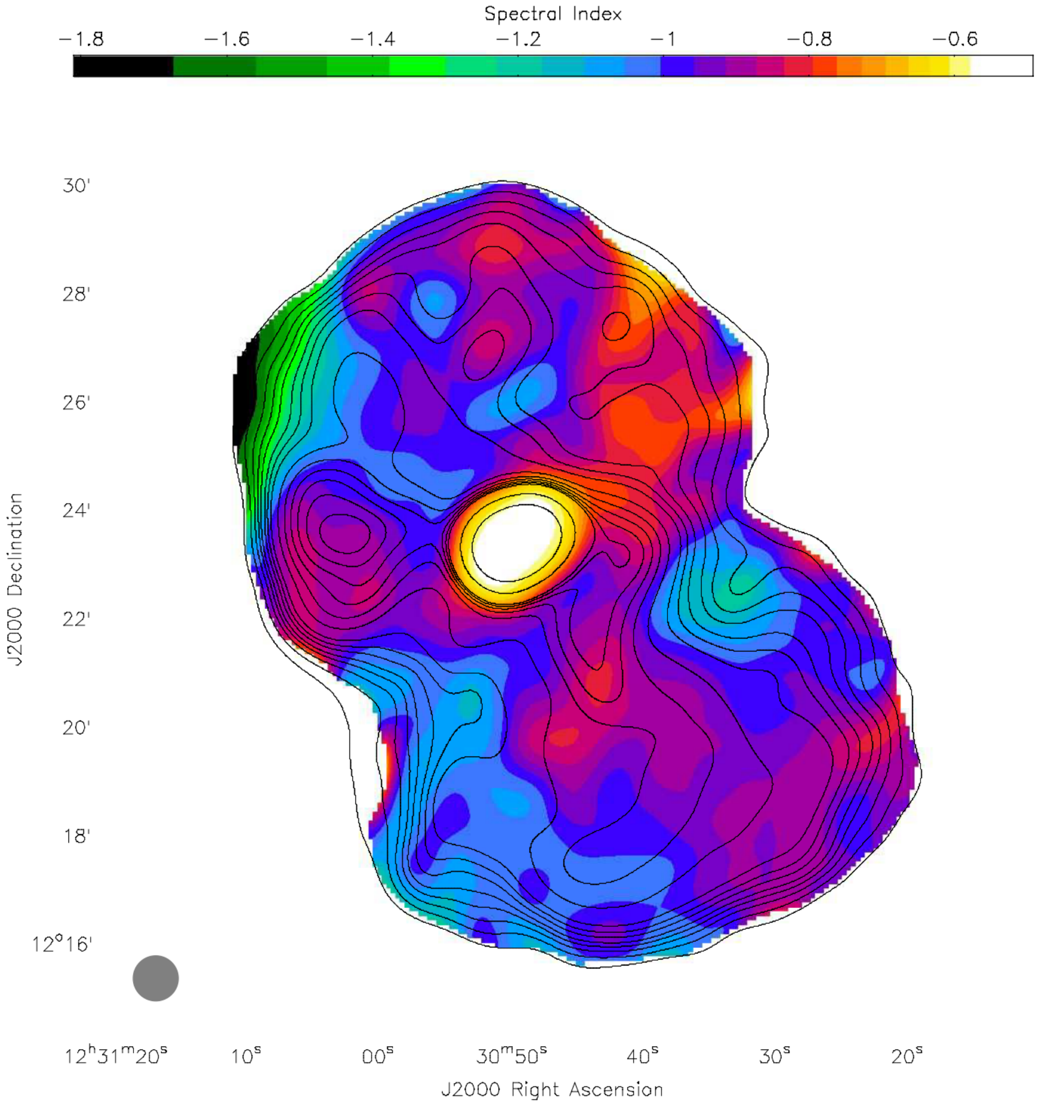

FIGURE 3.8: The LOFAR M87 spectral index map. This was obtained from LOFAR LBA in the range 45-71 MHz and LOFAR HBA in the range 115-162 MHz, this also makes use of the VLA map at 325 MHz. All maps were convolved to a resolution of 50 arcsec. The image was made by pixel-by-pixel linear regression was model. Contours are generated from the the 325 MHz map. (de Gasperin et al., 2012).

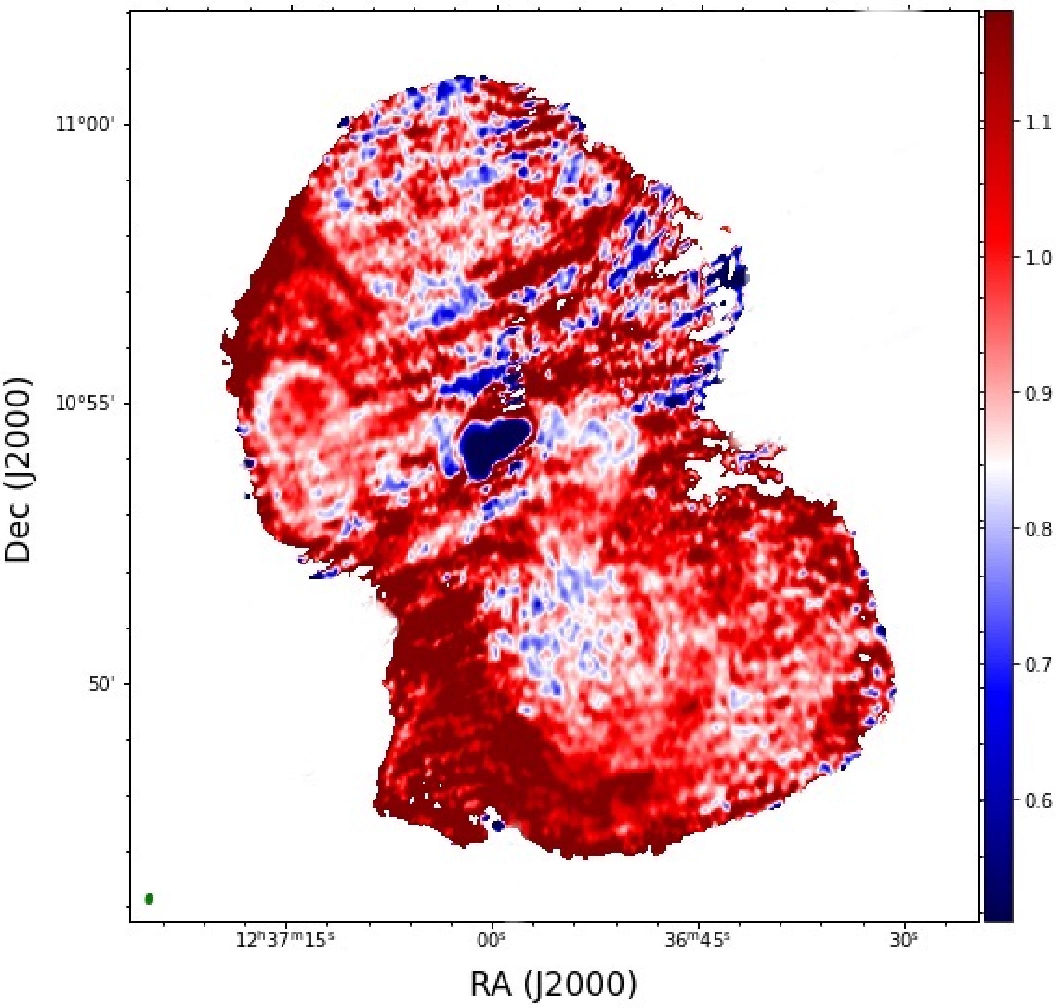

FIGURE 3.9: A lo-band (1026-1250 MHz) MeerKAT spectral index map of M87. The various maps we smoothed to a beam size of 13arcsec × 8arcsec. Pixel values below 5σ were excluded.

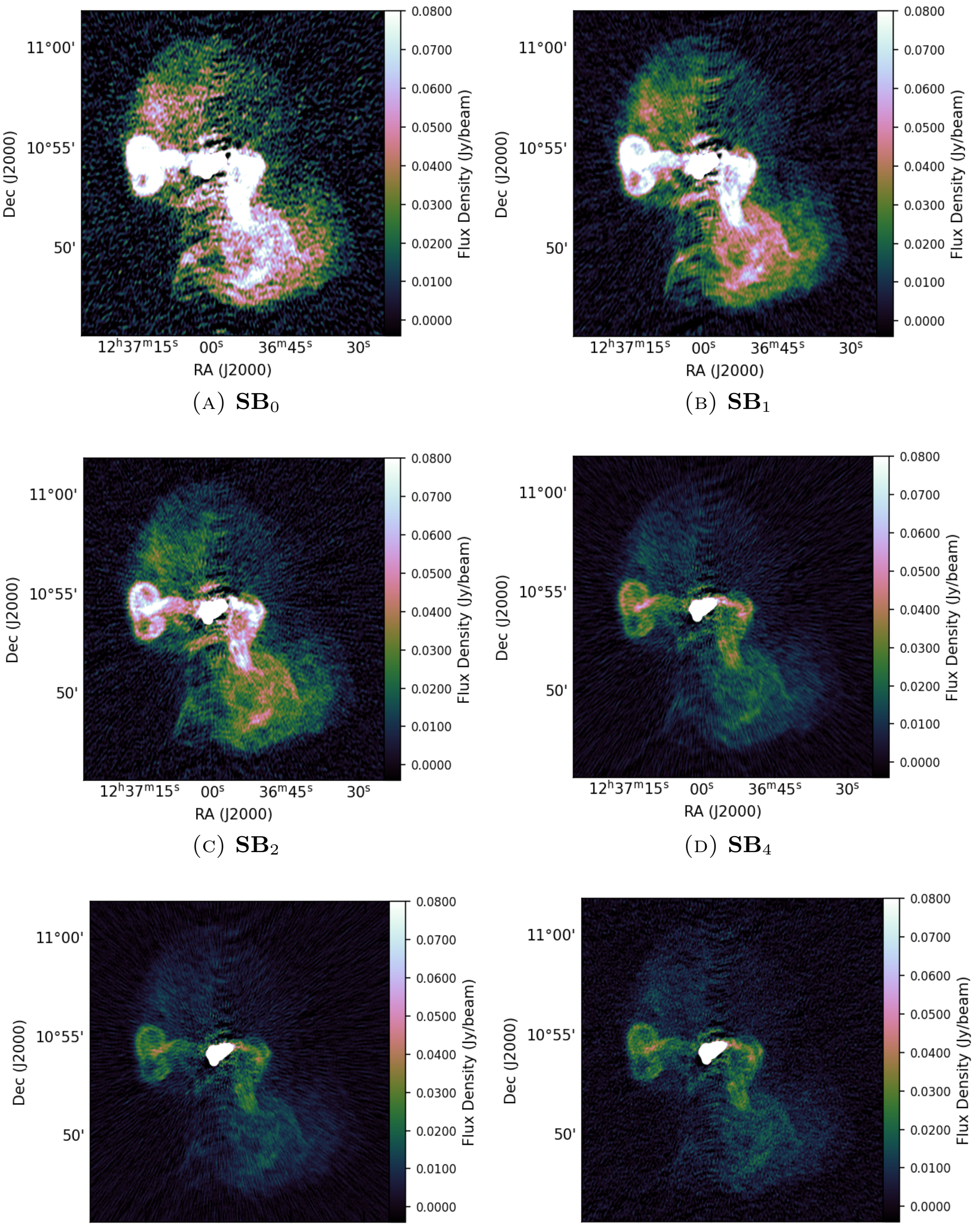

(A) $\mathbf{SB}_0$ (B) $\mathbf{SB}_1$

(C) $\mathbf{SB}_2$ (D) $\mathbf{SB}_4$

(E) $\mathbf{SB}_5$ (F) $\mathbf{SB}_6$

FIGURE 3.10: The sub-images generated from the fractional frequency MeerKAT sub-bands.

The M87 integrated flux densities over all sub-bands was measured by the `CASA` task `imfit` and plotted against the corresponding frequencies. We fit the log-log space model of the form,

$$\log(S) = \log(b_0) - \alpha \log(\nu), \tag{3.1}$$

where α is the slope of the linear fit, ν the observing frequency, $\log(b_0)$ the y-intercept, S the observed flux (refer to Fig. 3.11). As previously noted, there is a general steepening of the spectral index the further we move from the core and as a result we observe a steeper, relative to the core spectral index, integrated spectral index of α_{909}^{1551}= -0.94 ±0.01.

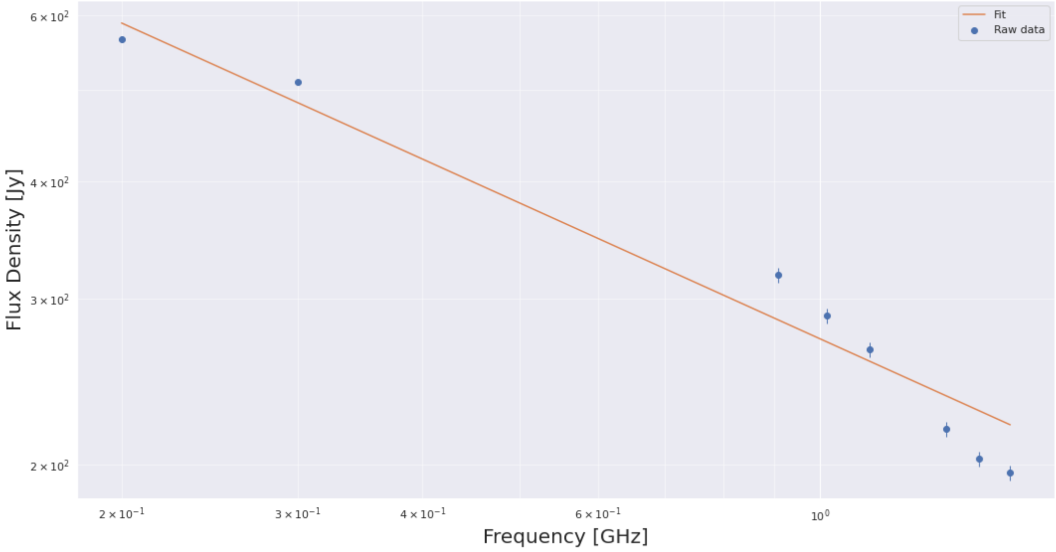

FIGURE 3.11: The integrated flux density of the entire halo of M87, taken at the various sub-band frequencies. The linear fit has a slope of α = -0.94 ±0.01, a y-intercept of 458 Jy and an average error of 1.23 Jy. We also made use of the NASA/IPAC Extragalactic Database for the first two data points in the plot. Error estimates were derived from the `CASA` task `imfit`, where we fit Gaussian components over various regions of the halo. This spectral index is consistent, on average, with the spectral index in Fig. 3.7.

The noise rms is plotted against the frequency in Fig. 3.12, in the same range as above. The noise, as a function of frequency traces the flux density as a function of frequency. This may be because the images are dynamic range limited, as opposed to being thermal noise limited, refer to the roughly constant dynamic range plot (and also Table 3.4) in Fig. 3.13, due to the combined effect of the calibration artefacts and the brightness of M87.

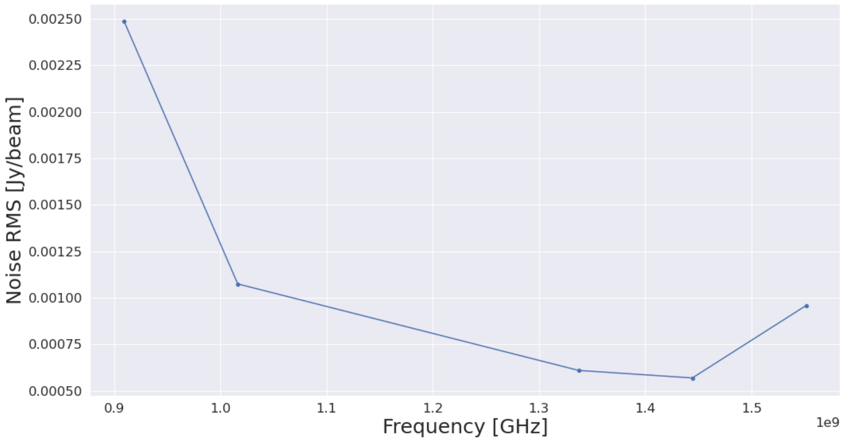

FIGURE 3.12: The channelised rms noise level as a function of frequency. A region was placed at a standardised position across the various sub-band images, away from the artefacts, and using `CARTA` statistics tool we measured the noise rms of each of the images.

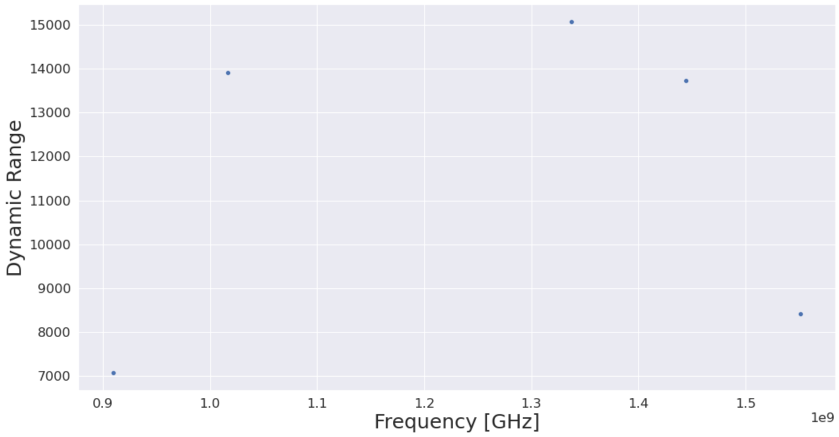

FIGURE 3.13: The image dynamic range as a function of frequency. The dynamic range is relatively constant, suggesting the images are dynamic range rather than thermal noise limited as suggested by the theoretical noise calculations presented earlier.

3.4 Minimum-energy requirements of M87

Following Owen et al. (2000), we label some key features of interest. When localised pressures increase, the charged particles occupy a smaller volume, i.e. move closer together, which in-turn causes the magnetic field lines that are associated with these charged particles to move closer and ultimately increasing the localised synchrotron power. This is referred to as having higher minimum-pressures and is the subject of this section. In Table 3.5 we give the results of minimum-pressure analysis from the filaments labeled A through F in Fig. 3.14.

In performing the analysis we made the following standard assumptions for the various regions of the halo,

1. The minimum magnetic field strength is at the equipartition energy.
2. The energy ratio k is evenly distributed across the electron-proton population, thus resulting in $U_{\text{proton}}/U_{\text{electron}} = k = 1$.
3. An observing frequency range of 10 MHz to 10 GHz.
4. An integrated spectral index of $\alpha =$ -0.94 ±0.01, as observed.
5. Assumed a rectangular geometry for each region with a depth equal to $d =$ (x + y)/2,here x and y are the long and short lengths of the region selected region, respectively.
6. Assume a luminosity distance of 17.9 Mpc (Gebhardt et al., 2011) and a redshift of $z = 0.004$.

To measure these elevated pressures we need to first obtain the magnetic field strength. The magnetic field cannot be directly derived from the total intensity synchrotron emission of a source, thus we consider the energy at equipartition, which is a reasonable approximation of the minimum-energy of the system. The minimum-energy (obtained from (Govoni & Feretti, 2004) for a synchrotron source is given by,

$$u_{\text{min}} = \xi(\alpha, \nu_1, \nu_2)(1+k)^{4/7}(\nu_0)^{4\alpha/7}(1+z)^{(12+4\alpha)/7} I_0^{4/7} d^{-4/7}, \tag{3.2}$$

where $\xi(\alpha, \nu_1, \nu_2)$ is a frequency depended variable, I_0 is the flux density of the source at the break frequency ν_0, d is the depth of the galaxy and z is the redshift of the galaxy[8].

---

[8] For the complete derivation we refer you to Govoni & Feretti (2004)

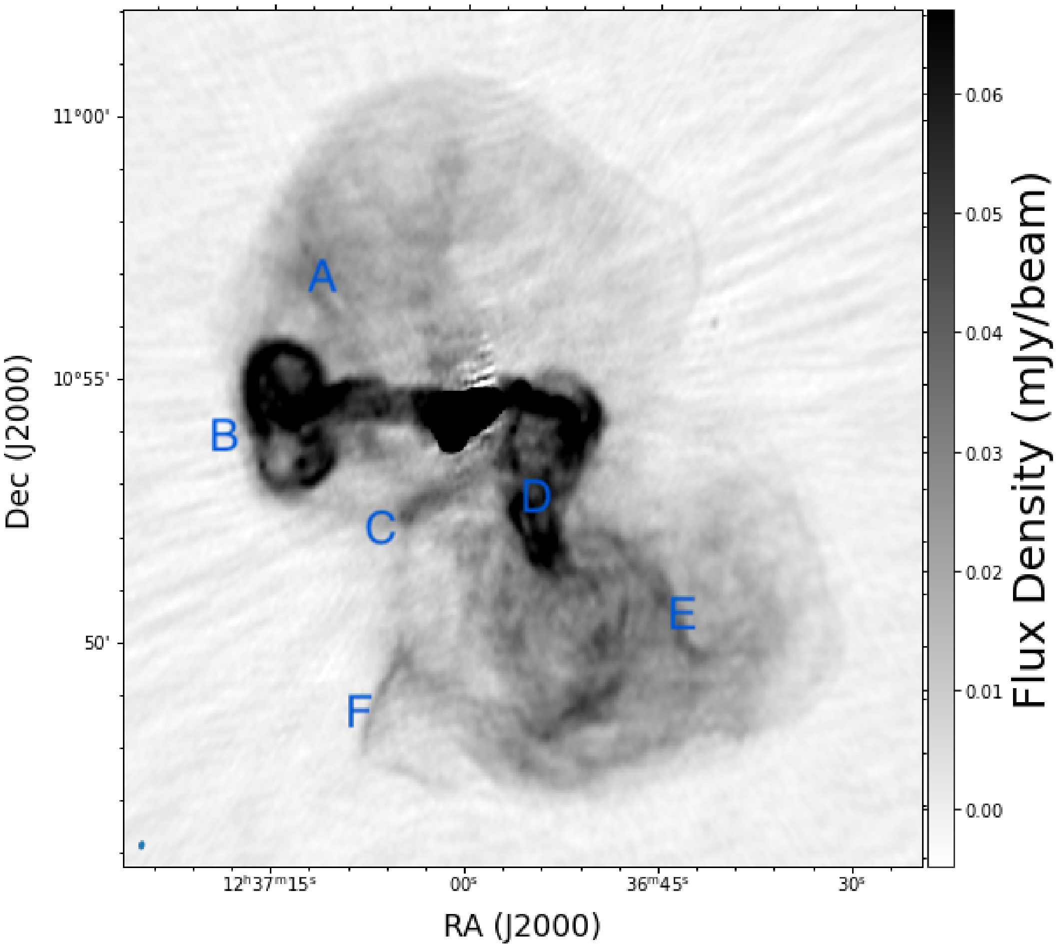

FIGURE 3.14: Fig. 3.1 re-plotted for the reader's convenience. This L-band gray-scale MeerKAT map of M87, highlights the regions of proposed elevated minimum pressures.

We measure an average spectral index of α = -0.94 ±0.01 over the entire M87 halo (refer to Fig. 3.11), set a proton-electron energy ratio of k = 1, i.e. the particle energy and used a $\xi(0.5, 10\,\mathrm{MHz}, 10\,\mathrm{GHz}) = 2.13\times10^{-12}$ in calculating the minimum energies[9]. The equipartition magnetic field is,

$$B_{\mathrm{min}} = \left(\frac{24\pi}{7}u_{\mathrm{min}}\right)^{\frac{1}{2}}. \tag{3.3}$$

From Condon & Ransom (2016) we obtain the minimum pressure calculation,

$$P_{\mathrm{min}} = \frac{13}{7\pi}B^2_{\mathrm{min}}. \tag{3.4}$$

The MeerKAT-derived minimum-pressure results in Table 3.5 are similar of the Owen et al. (2000) values.

---

[9] For a list of values see (Govoni & Feretti, 2004).

Feature	Integrated Flux Density [Jy]	Min. Energy [10^{-13} erg/cm^3]	Min.B Field [μG]	Min. Pressure [10^{-12} dyne cm^{-2}]
A	14	3.37	1.90	2.06
B	3.3	4.00	2.08	2.44
C	2.5	3.96	2.06	2.42
D	6.8	3.72	2.00	2.27
E	1.4	1.80	1.39	1.10
F	32.	2.47	1.63	1.51

Table 3.5: Minimum-Pressure analysis for the filamentary features of M87 as labelled in Fig.3.14. This table is reminiscent of Table 1 of Owen et al. (2000).

3.5 Synchrotron lifetime of M87

Particles in a synchrotron halo are, in general, losing energy. The time scale for this to occur is given by the ratio of the energy of the particles to the power at which they are radiating away their energy.

Recall, that in quantifying the morphological features of a radio galaxy, we are required to make simplifying assumptions. We assume that the field strength and the number density are constant over localised areas. In reality there are variations in the structure of the emission observed.

We shall use two results to compute the synchrotron age of the M87 halo. Taking the redshift to be z=0.004, the minimum magnetic field strength to be $B = 1.84$ μG, the break frequency $\nu_{\mathrm{syn}} = 1.3$ GHz and the Compton scattering $\sigma_T = 6.65\mathrm{e}29$ m^2. Using Eq. 1.17, we calculate the synchrotron lifetime of the M87 radio halo to be $\mathrm{t}_{\mathrm{cool}} = 1 \times 10^8$ **yr**, at the the average value of 1 μG over the whole halo. Using the result from Murgia et al. (2011),

$$t_{\mathrm{s}} = 1590 \frac{B^{0.5}}{(B^2 + B^2_{\mathrm{CMB}})[(1+\mathrm{z})\nu]^{0.5}}, \tag{3.5}$$

where the symbols have the same meaning as in Sec. 1.2.4. We obtain the following $\mathrm{t}_{\mathrm{s}} = 1.36 \times 10^8$ **yr**. The above two calculations give similar values. However, our results stray quite far from those found by de Gasperin et al. (2012) by an order of magnitude. They, however, do differ in their initial assumptions, they select different low-energy cut-off, spectral slope and model for their synchrotron emissivity, which does account for the discrepancy.

Chapter 4

Summary and Future Prospects

It has been our goal to generate a full-bandwidth map of M87 with the MeerKAT telescope at 1.3 GHz and to compare it with the VLA 327 MHz map of M87. In our comparison we have observed some remarkable similarities in the the two images, despite the differences in the observing frequencies and imaging software used. Two things of note are **1**) M87 is a northern source and **2**) the data was obtained during the commissioning of MeerKAT. These two factors posed a bigger challenge in our reduction than we initially anticipated.

The imaging software `WSClean` was used to image the MeerKAT data and Owen et al. (2000) used `VTESS` to make the VLA map. `VTESS` leverages the maximum Entropy method in making its images. `WSClean` uses the w-stacking algorithm. The main differentiating properties of the imaging software is that `VTESS` images have not been convolved with a beam and no residual is added to the restored map. At both small and large scales, the VLA and MeerKAT images of the M87 halo appear to have an uncanny resemblance, from the over-saturated core to the diffuse halo.

The halo is quite complex with a network of filaments emerging from the core extending into diffuse emission. Despite having the, essentially, same structure between the two maps, the M87 regional brightnesses were quite different. It is unknown whether the filaments are due to strong magnetic fields or higher particle numbers in these localised regions. Some things of note about the physical structure,

1. No emission beyond the sharp edges of the halo is ever seen.
2. No relationship between the spectral index and the brightness of the galaxy.
3. The halo boundary is at a pressure balance with the ICM (Owen et al., 2000).

The large scale radio halo of M87 has been imaged at 25 MHz (de Gasperin et al., 2012), 327 MHz (Owen et al., 2000) and now at 1.28 GHz. At these frequencies the M87 morphology appears to be quite similar. This fact, coupled with the observation that there is no emission beyond the edge-brightened boundary of the halo, implies that the halo emission is relatively fresh and that there is a continuous injection of relativistic electrons from the AGN (de Gasperin et al., 2012). Had the emission been a relic, we would have observed a strong frequency dependence in the structure over this broad frequency range.

We've computed a two point spectral index image from the MeerKAT and VLA total intensity maps, between 327 MHz and 1.28 GHz. Even though a general steepening was observed in the halo, there was no evidence of a relationship between the spectral index and brightness, a point which was also made by de Gasperin et al. (2012).

An in-band spectral index map was created owing to the large fractional bandwidth of MeerKAT. Six points within the MeerKAT L-band were used to generate the map. Even in this map no striking features were observed, there was indeed a steepening of the spectral index as we moved further from the core, but no noteworthy relationship was discovered. To summarise, we have achieved our goal to,

1. Generate a full-bandwidth map of M87.
2. Study its large-scale radio lobes an halo.
3. Conduct a detailed comparison between the MeerKAT 1.3 GHz and the VLA 327 MHz map.
4. Make a MeerKAT in-band spectral index map of M87.

In these results we draw a surprising, but consistent conclusion. The M87 structure shows a remarkably low spectral variation over quite a large range of frequencies. It is our opinion that another observation of the source at UHF would potentially reveal structure which we couldn't detect. We detect what we suspect to be a thread at the structure C in Fig 3.14. In addition we calculate the synchrotron age of the M87 halo using two methods and we find it to be approximately 118 Myr.

We intend to improve on the results presented in this dissertation for our publication in preparation. Our next goal is to go even further in the process of self-calibration, by improving the flagging, imaging and calibration parameter space. To further explore the interconnectedness of the X-ray and radio emissions of M87. As a final note, HI observations may be possible, which would give a better understanding of the galaxy's evolution.

Appendix A

Appendices

A.1 Large-scale Extended Radio Emission in M87

Visibility tapering can be used to modify the shape of the synthesized beam, by "down-weighting" the uv-sampling on long baselines. This task improves the shape of the beam, but at a loss of spacial resolution.

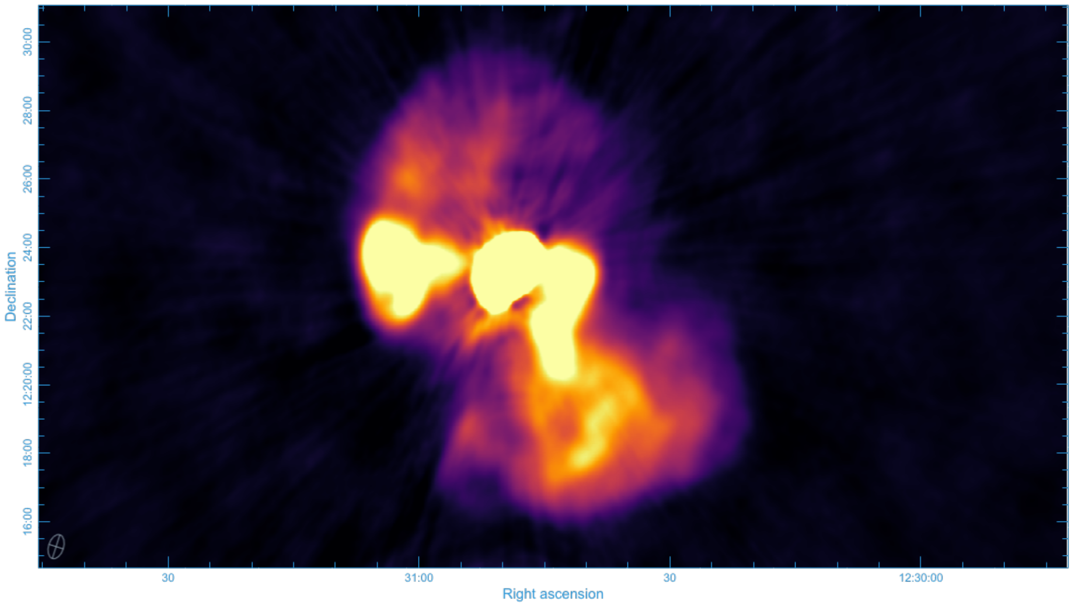

Figure A.1: Phase selfcal image with 13 arcsec tapering

Figure A.1 and Figure A.2 correspond to our phase-only and amplitude and phase calibrated 13 arcsec taper images.

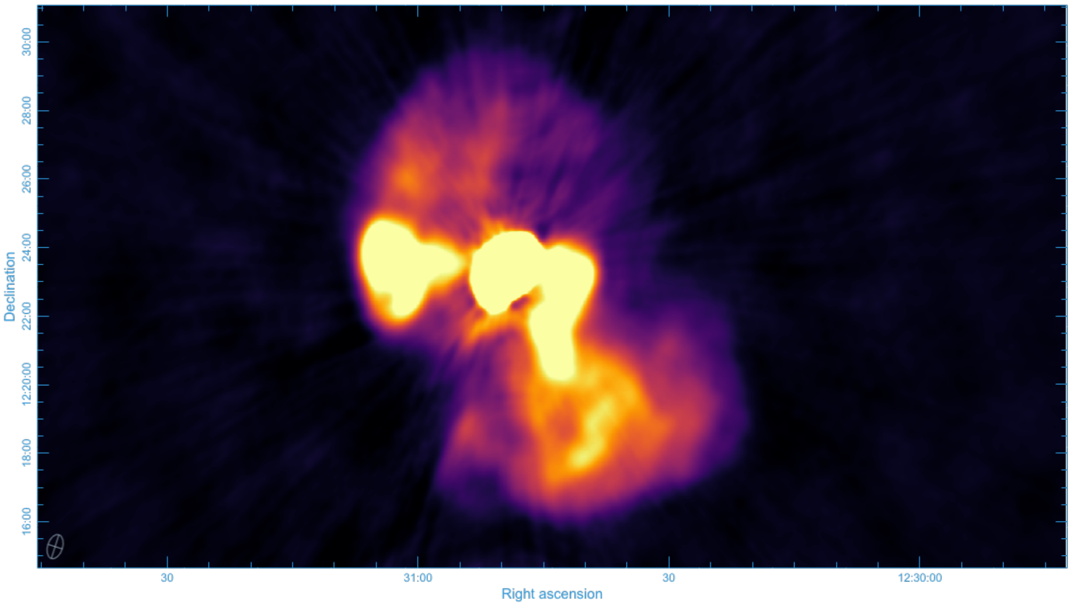

Figure A.2: Amplitude and phase selfcal image with 13 arcsec tapering

A.2 Montage From Conference 2020

Figure (A.3) is a montage of the various regions of interest in the MeerKAT M87 galactic structure. The left most image shows the full extend of the galaxy, with some key structures labelled. The top insert is a zoomed in clip of the inner regions, i.e. the outflows that emerge from the inner most region of the galaxy. Finally, the lower insert image shows the cocoon region, that constitutes the central engine and the two collimated jets.

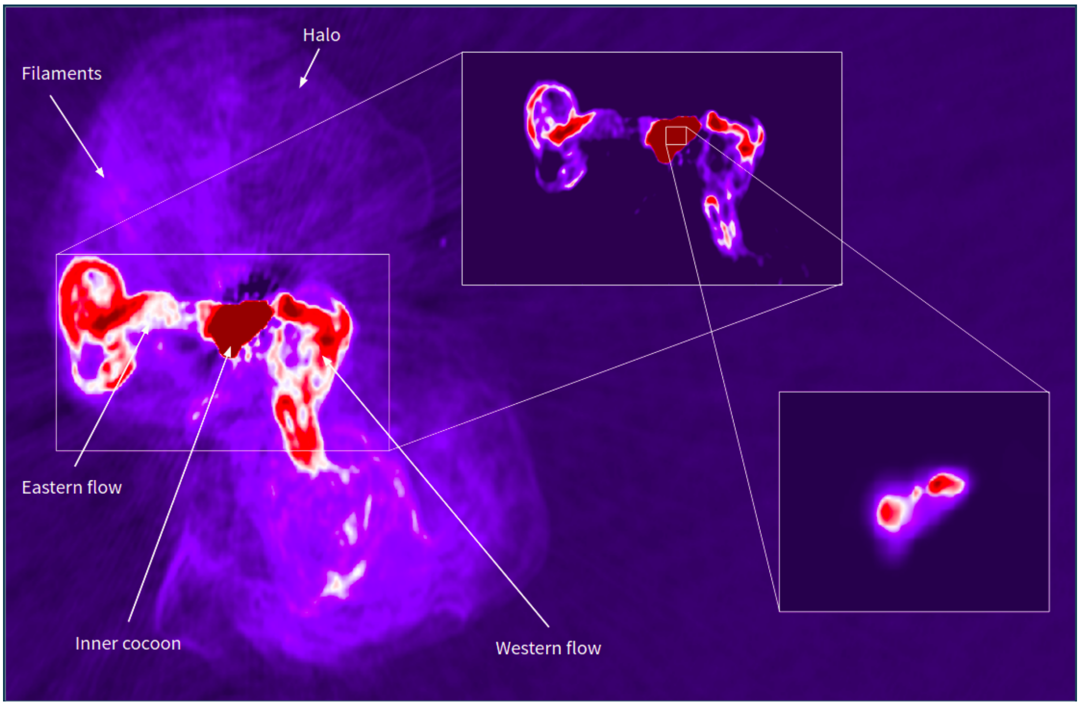

Figure A.3: (Main): MeerKAT full bandwidth image of M87 at 1.28 GHz. We observed flair-like features, north of the core region (final imaging strategy is still in progress). Beam size 24 x 16 arcsec, rms noise level $\sigma = 24$ mJy/beam. Following de Gasperin et al. (2012) we label key features in the M87 extended structure. Top-right Insert: A close up of the core and eastern and western outflows. The sharp drops in surface brightness between the inner these lobes and core are prominent. Bottom-right Insert: Full color range of M87 showing only the core

A.3 A CLEAN Algorithm Model

Figure (A.4) shows a WSClean obtained model by imaging self-calibrated M87 data, with Multi-scale clean. As can be seen the model has a mottled structure, this is caused by the assumptions made in the operation of the CLEAN algorithm.

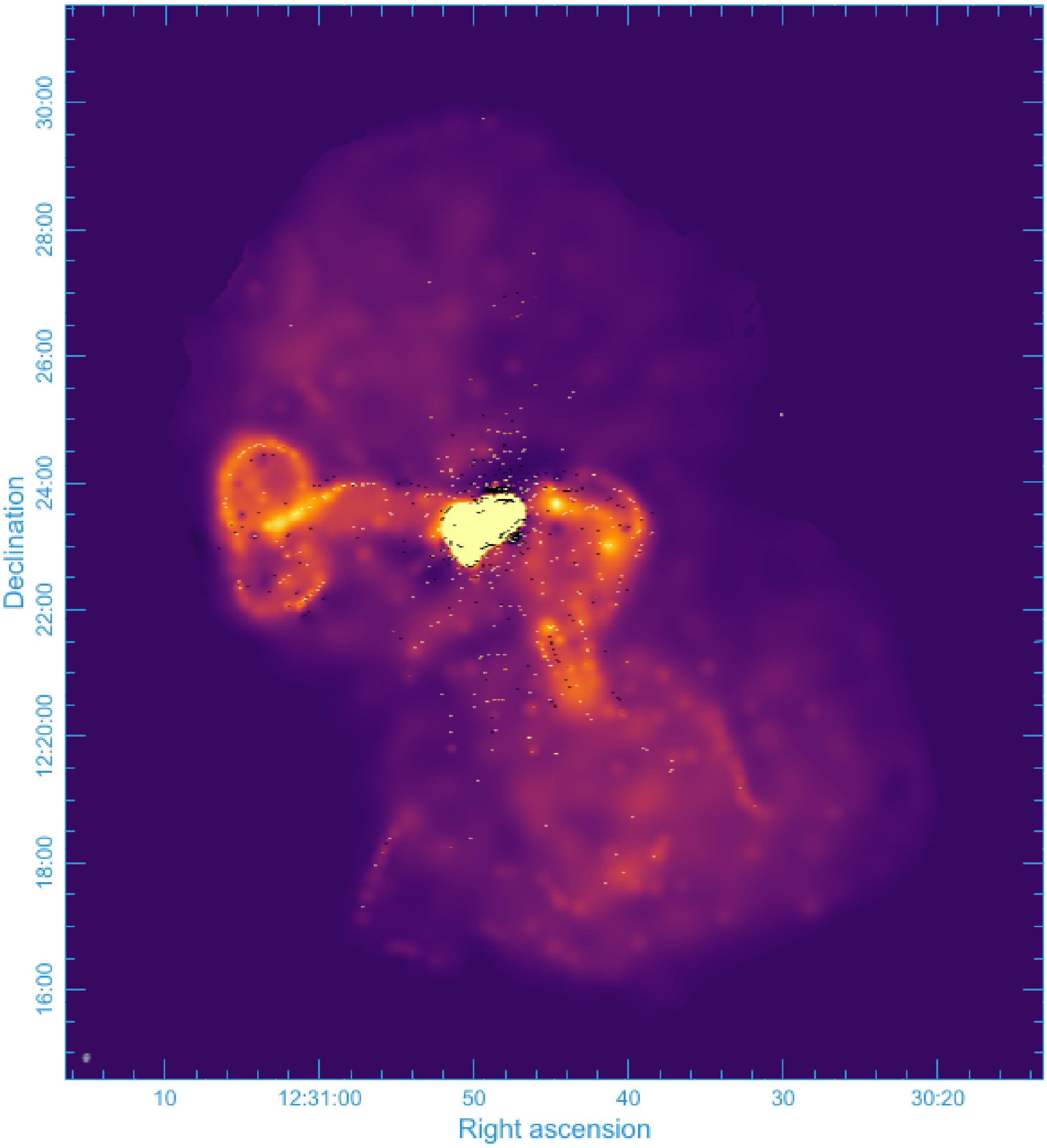

FIGURE A.4: An M87 `WSClean` model. This model shows the typical inaccuracies that `WSClean` are known to have, nonphysical bright spots.

Bibliography

Antonuccio-Delogu, V., Cielo, S., Silk, J., & Romeo, A. 2017, Monthly Notices of the Royal Astronomical Society, 467, 4526

Ascasibar, Y., & Markevitch, M. 2006, The Astrophysical Journal, 650, 102–127

Baars, J. W. M., Genzel, R., Pauliny-Toth, I. I. K., & Witzel, A. 1977, aap, 500, 135

Blandford, R., Meier, D., & Readhead, A. 2019, Annual Review of Astronomy and Astrophysics, 57, 467–509

Bohringer, H., Nulsen, P. E. J., Braun, R., & Fabian, A. C. 1995a, Monthly Notices of the Royal Astronomical Society, 274, L67

—. 1995b, Monthly Notices of the Royal Astronomical Society, 274, L67

Burns, J. O. 1990, aj, 99, 14

Churazov, E., Brüggen, M., Kaiser, C. R., Böhringer, H., & Forman, W. 2001, , 554, 261

Churazov, E., Forman, W., Jones, C., & Bohringer, H. 2000, arXiv preprint astro-ph/0002375

Condon, J. J., Cotton, W. D., White, S. V., et al. 2021, The Astrophysical Journal, 917, 18

Condon, J. J., & Ransom, S. M. 2016, Essential Radio Astronomy

Cornwell, T. J. 2008, IEEE Journal of Selected Topics in Signal Processing, 2, 793

de Gasperin, F., Orrú, E., Murgia, M., et al. 2012, A&A, 547, A56

Ertley, C. 2014

Event Horizon Telescope Collaboration, Akiyama, K., Alberdi, A., et al. 2019a, , 875, L4

—. 2019b, , 875, L4

Fabian, A. C. 1994, , 32, 277

Fabian, A. C., Sanders, J. S., Ettori, S., et al. 2000, , 318, L65

Fabricant, D., Lecar, M., & Gorenstein, P. 1980, apj, 241, 552

Fanaroff, B. L., & Riley, J. M. 1974, mnras, 167, 31P

Forman, W., Jones, C., Churazov, E., et al. 2007, The Astrophysical Journal, 665, 1057

Fouqué, P., Solanes, J. M., Sanchis, T., & Balkowski, C. 2001, Astronomy 'I&' Astrophysics, 375, 770–780

Garofalo, D., Evans, D. A., & Sambruna, R. M. 2010, Monthly Notices of the Royal Astronomical Society, 406, 975

Gebhardt, K., Adams, J., Richstone, D., et al. 2011, , 729, 119

Gebhardt, K., & Thomas, J. 2009, The Astrophysical Journal, 700, 1690

Gopal-Krishna, & Wiita, P. J. 2000,
aap, 363, 507

Govoni, F., & Feretti, L. 2004, International Journal of Modern Physics D, 13, 1549–1594

Harwood, J. J., Hardcastle, M. J., & Croston, J. H. 2015, Monthly Notices of the Royal Astronomical Society, 454, 3403

Harwood, J. J., Hardcastle, M. J., Croston, J. H., & Goodger, J. L. 2013, Monthly Notices of the Royal Astronomical Society, 435, 3353

Heald, G., McKean, J., Pizzo, R., et al. 2010, Progress with the LOFAR Imaging Pipeline

Herbig, T., & Readhead, A. 1992, The Astrophysical Journal Supplement Series, 81, 83

Heywood, I. 2020, oxkat: Semi-automated imaging of MeerKAT observations

Jaffe, W. J., & Perola, G. C. 1973, , 26, 423

Jonas, J. L. 2009, Proceedings of the IEEE, 97, 1522

Kaiser, C. R., & Alexander, P. 1997, mnras, 286, 215

Kassim, N. E., Perley, R. A., Erickson, W., & Dwarakanath, K. S. 1993, aj, 106, 2218

Kellermann, K., Kovalev, Y., Lister, M., et al. 2007, Astrophysics and Space Science, 311, 231

Kellermann, K. I., & Verschuur, G. L. 1988, Galactic and Extragalactic Radio Astronomy

Kovalev, Y. Y., Lister, M. L., Homan, D. C., & Kellermann, K. I. 2007, The Astrophysical Journal, 668, L27

Leahy, J. P., & Williams, A. G. 1984,
mnras, 210, 929

Longair, M. 2011, High Energy Astrophysics (Cambridge University Press)

Makhathini, S. 2018, PhD thesis, Rhodes University, Drosty Rd, Grahamstown, 6139, Eastern Cape, South Africa, available via http://hdl.handle.net/10962/57348

Mantz, A. B., Allen, S. W., Morris, R. G., et al. 2017, Monthly Notices of the Royal Astronomical Society, 472, 2877–2888

Markevitch, M., & Vikhlinin, A. 2007, Physics Reports, 443, 1–53

McNamara, B. R., & O'Connell, R. W. 1993, , 105, 417

Murgia, M., Parma, P., Mack, K.-H., et al. 2011, Astronomy & Astrophysics, 526, A148

Mushotzky, R. F., Serlemitsos, P. J., Smith, B. W., Boldt, E. A., & Holt, S. S. 1978, apj, 225, 21

Myers, S. T., & Spangler, S. R. 1985, , 291, 52

Narayan, R., Igumenshchev, I. V., & Abramowicz, M. A. 2003, Publications of the Astronomical Society of Japan, 55, L69

Offringa, A. R., & Smirnov, O. 2017, MNRAS, 471, 301

Offringa, A. R., van de Gronde, J. J., & Roerdink, J. B. T. M. 2012, A&A, 539, A95

Owen, F. N., Eilek, J. A., & Kassim, N. E. 2000, The Astrophysical Journal, 543, 611

Pacholczyk, A. G. 1970, Radio astrophysics. Nonthermal processes in galactic and extragalactic sources

Pacholczyk, A. G. 1970, Radio astrophysics. Nonthermal processes in galactic and extragalactic sources

Peterson, J., & Fabian, A. 2006, Physics Reports, 427, 1

Pfrommer, C., & Jones, T. W. 2011, , 730, 22

Ramatsoku, M., Murgia, M., Vacca, V., et al. 2020, A&A, 636, L1

Rau, U., & Cornwell, T. J. 2011, aap, 532, A71

Rybicki, G. B., & Lightman, A. P. 1986, Radiative Processes in Astrophysics, 400

Sarazin, C. L. 1986, Reviews of Modern Physics, 58, 1

The GIMP Development Team. 2019, GIMP

Turland, B. D., & Scheuer, P. A. G. 1975, Monthly Notices of the Royal Astronomical Society, 170, 281

Turner, R. J., & Shabala, S. S. 2015, The Astrophysical Journal, 806, 59

van Haarlem, M., Wise, M., Gunst, A., et al. 2013, Astronomy & Astrophysics, 556, A2

Walsh, J. L., Barth, A. J., Ho, L. C., & Sarzi, M. 2013, , 770, 86

Walters, J., & Davidson, J. 1963, Journal of Fluid Mechanics, 17, 321

Wilson, T. L., Rohlfs, K., & Hüttemeister, S. 2013, Tools of Radio Astronomy